

**FACULDADE DE ENGENHARIA DA UNIVERSIDADE DO PORTO
INSTITUTO DE CIÊNCIAS BIOMÉDICAS ABEL SALAZAR**

3D Modeling Applied to the Manufacture of Personalized Bioceramic Medical Devices

Maria Inês Mora Martins

DISSERTATION FOR THE DEGREE OF MASTER IN BIOENGINEERING

MSC IN BIOENGINEERING - MOLECULAR BIOTECHNOLOGY

Supervisor: Maria Ascensão Lopes, PhD.

Co-supervisor: José Domingos Santos, PhD.

28th February

© Inês Martins, 2019

This work has been performed under a non-disclosure agreement with a medical device company and, therefore, some details of the process have been omitted.

3D Modeling Applied to the Manufacture of Personalized Bioceramic Medical Devices

Maria Inês Mora Martins

MSC IN BIOENGINEERING - MOLECULAR BIOTECHNOLOGY

28th February

Resumo

A perda de tecido ósseo é um profundo problema clínico atual e, estando diretamente associado ao envelhecimento populacional, promove a intensa expansão do mercado de enxerto ósseos.

Uma vez que o uso de auto-, alo- e xeno-enxertos começa a ser posto em causa devido às complicações associadas, o foco da investigação em regeneração óssea está a voltar-se para alternativas sintéticas, mais especificamente aquelas à base de materiais biocerâmicos. No entanto, os produtos atualmente disponíveis no mercado não alcançam os requisitos necessários nomeadamente os referentes à arquitetura tridimensional do produto uma vez que não permitem uma combinação morfológica perfeita entre o material e o defeito existente.

Nesta dissertação, uma nova abordagem é explorada para produzir enxertos ósseos sintéticos que mimetizam a complexa estrutura óssea usando tecnologia de fabricação aditiva de impressão por processamento digital de luz.

Partindo de um modelo virtual, gerado através de desenho computacional, os parâmetros de impressão foram otimizados para o processo de impressão usado.

Estruturas com níveis de porosidade de 90% foram produzidas por incorporação de pós de hidroxiapatite numa resina fotocurável à base de metacrilatos, dando origem a uma suspensão que pode ser impressa. Com esta técnica, pequenas quantidades de suspensões foram polimerizadas através de exposição luminosa, produzindo, numa abordagem de camada-a-camada, uma estrutura que replica qualquer modelo virtual, possibilitando assim a criação de estruturas de morfologia complexa e um controlo total da sua geometria.

Após impressão, as peças foram submetidas a um processo de sinterização bifásico. Na primeira fase, a queima da resina assegura a segurança biológica do enxerto ósseo que deve estar livre de resíduos de resina. Num segundo passo, ocorre o processo de sinterização que favorece um melhoramento das propriedades mecânicas do enxerto.

Foram testadas diferentes formulações que variavam quer na quantidade de pó incorporada como na origem do pó. As impressões apenas foram bem sucedidas quando usando suspensões preparadas a partir de pós de hidroxiapatite de fase pura. Após sinterização, verificou-se uma pequena transformação de fase, na ordem dos 10%, de hidroxiapatite em α -fosfato tricálcico. Isto deve-se à presença de resíduos de Silício após queima da resina que destabilizam a estrutura da hidroxiapatite.

Graças ao efeito sinérgico do grande tamanho de poros das estruturas tridimensionais e o limite máximo de incorporação de sólidos determinado pelo valor de viscosidade, as peças produzidas apresentaram alguma fragilidade. Como solução, foi explorado um método de imersão do enxerto em biovidro para melhorar as suas propriedades mecânicas. No entanto, apesar das peças resultantes demonstrarem níveis de resistência superiores, altos níveis de transformação de fase foram registados. A sua composição final consistiu praticamente na totalidade em α -fosfato tricálcico que se irá traduzir numa taxa de degradação mais rápida quando implantado.

Abstract

Bone tissue loss consists in a major clinical issue and being deeply connected to the consistent population aging, bone graft market is clearly expanding enormously.

As auto-, allo- and xenografts are no longer appealing due to their associated complications, the attention is turning towards the synthetic alternatives bioceramic based materials. However, the currently available bioceramic products are not completely satisfactory as they do not allow a perfect match to the bone's defect morphology, in terms of its three dimensional architecture.

In this dissertation, a novel approach is explored to produce synthetic bone grafts mimicking the complex bone structure using additive manufacturing digital light processing technology.

Starting from a virtual scaffold model that was constructed through computer assisted design, the printable settings were optimized for the chosen three dimensional printing process for the development of this work.

Structures with a 90% pore content were produced by incorporating hydroxyapatite powders in a methacrylated based photocurable resin, creating a printable suspension. With this technique, small amounts of suspensions were polymerized upon light exposition at a time, producing, in a layer-by-layer approach, a structure that replicates any designed virtual model, being possible to generate scaffolds with complex morphology and total geometrical control.

After printing, the three dimensional pieces were submitted to a two-step sintering cycle. In the first step, the resin burn-out occurs, ensuring the biological safety of the bone graft that must be free of resin residues. In the second step, the sintering process takes place to enhance the scaffold's mechanical properties.

Different suspensions' formulations, varying on the powder content as well as on the hydroxyapatite powder provider were tested. However, successful prints were attained only for those ones prepared from pure phase hydroxyapatite powder. After sintering, a small phase transformation of hydroxyapatite into α -tricalcium phosphate in the 10% order occurred, probably due to the hydroxyapatite's structure destabilization promoted by the presence of the resin's silicon residues after burn-out.

Due to the synergic effect of the large pores of the produced structures and the maximum powder load incorporation imposed by the allowed viscosity range for printable suspensions, the produced structures were fragile. As a solution to overcome their weak mechanical properties, a bioglass immersion method was explored. However, the resulting three dimensional pieces, despite showing much better mechanical resistance, exhibited high levels of crystallographic phase transformation during sintering, and their final composition was mostly α -tricalcium phosphate which will translate on a higher dissolution rate of these scaffolds when implanted.

Agradecimentos

Finalmente, dando por terminado aquele que, até agora, foi o maior desafio na minha vida, resta-me apenas agradecer.

Aos meus professores, Maria Ascensão Lopes e José Domingos Santos, dirigo o mais sincero dos agradecimentos pela grande oportunidade que me ofereceram e por toda a ajuda, disponibilidade e preocupação demonstrados ao longo destes últimos meses que permitiram desenvolver este trabalho de que tanto me orgulho.

Ao Dr. Rui Coelho, pela confiança e pela paciência demonstrada no esclarecimento de todas as dúvidas que foram surgindo à medida que este projecto avançava.

A todas as minhas companheiras do F201, a quem agora chamo de amigas, o meu obrigado por todas as conversas e brincadeiras nos momentos de distração e, especialmente, por todo o apoio nos períodos menos bons.

Às meninas da Maia, obrigada por todos os "cafés" e todos os outros momentos que me enchem de alegria e carinho.

A todos os que ocupam o meu coração e que transformaram esta aventura nos melhores anos da minha vida. Obrigada aos de Bio, aos de Metal, aos da FEUP, aos do ICBAS, aos de 2013, aos mais velhos e aos mais novos.

Finalmente, o agradecimento indispensável. Obrigada aos meus pais, do fundo do coração, por toda a educação e amor. Sem eles, nada teria sido possível.

Inês

“We are the dead. Our only true life is in the future.”

George Orwell

Contents

Abbreviations	xv
1 Introduction	1
1.1 Contextualization	1
1.2 Motivation and objective	3
2 Background and literature review	5
2.1 The Bone	5
2.2 Porous ceramics	10
2.3 Modelling and Three Dimensional Printing	16
3 Materials and Methods	21
3.1 3D Printer	21
3.2 Raw Materials	22
3.3 Formulations	23
3.4 Material characterization	24
4 Modeling and 3D Printing	29
4.1 Post-printing procedure	32
5 Results and discussion	35
5.1 Resin	35
5.2 Hydroxyapatite powders	39
5.3 Formulations	42
5.4 3D printed pieces	44
6 Conclusions and Future Work	53
References	55

List of Figures

1.1	Global bone grafts market share	2
2.1	Representation of different bone types: cortical and trabecular	6
2.2	The bone remodeling sequence	9
2.3	Correspondence between ceramic pore size and applications	11
2.4	Possible processing routes used for the production of porous ceramics	13
2.5	The seven categories of additive manufacturing processes	18
2.6	Examples of bone models.	19
3.1	The working principle of DLP printing	21
3.2	Molecular structure of sodium dodecyl sulphate	23
3.3	3D porous sample prepared for scanning electron microscopy	27
4.1	Original trabecular structure for model design	29
4.2	Different virtual models originated from the same original file	30
4.3	Outcome of the support generation process	31
4.4	Different cross sections of a model for 3D printing	32
4.5	Heating curve for firing treatment of 3D printed pieces	33
4.6	Visual representation of the post-printing procedure applied to a piece	34
5.1	Fourier-transform infrared spectroscopy spectrum of the resin	35
5.2	Resin's thermogravimetric analysis curve	37
5.3	Energy dispersive X-ray spectroscopy results of the resin analysis	38
5.4	Granulometric analysis of the HA powders	39
5.5	Scanning electron microscopy images for morphology assessment of different HA powders	39
5.6	Combined diffractogram of the two HA powders analysed trough XRD	40
5.7	Treated data concerning the viscosity determination of the different formulations	43
5.8	Post-sintering 3D printed piece	44
5.9	Pre-sintering 3D printed pieces	45
5.10	Combined diffractogram of a printed formulation and the respective calcined powder analyzed trough XRD	45
5.11	Post-sintering 3D pieces for porosity assessment	47
5.12	Scanning electron microscopy images for bioglass incorporation assessment	49
5.13	Combined diffractogram of a printed formulation and the respective bioglass immersed piece analyzed trough XRD	49
5.14	Combined diffractogram of a bioglass immersed piece and the respective piece for sintering control analyzed trough XRD	50

List of Tables

1.1	Classification of bone graft donor site complications	2
2.1	Vital statistics of adult bone remodeling	8
2.2	Several calcium phosphates and their respective Ca/P atomic ratios	15
3.1	Composition discrimination of the different printable prepared suspensions	24
5.1	FTIR peak assignment for the resin sample	36
5.2	Obtained results for the organic-inorganic relative composition analysis of the resin	37
5.3	Inorganic Crystal Structure Database referenced informations for the analysis of the obtained diffractograms	41
5.4	Identification of cristallographic phases and their relative contribution for the composition of each HA powder	41
5.5	Zeta potential value for the different HA powders	42
5.6	Identification of cristallographic phases and their relative contribution for the composition of the printed piece	46
5.7	Contraction values of 3D printed pieces after firing	46
5.8	Reported theoretical density values for the different cristallographic phases	47
5.9	Porosity evaluation results	48
5.10	Identification of cristallographic phases and their relative contribution for the composition of the bioglass immersed printed piece	50
5.11	Identification of cristallographic phases and their relative contribution for the composition of the printed piece for sintering control	50

Abbreviations

3D	Three Dimensional
AM	Additive Manufacturing
BMU	Basic Multicellular Unit
CAD	Computer Assisted Design
CT	Computed Tomography
DLP	Digital Light Processing
EDS	Energy Dispersive X-Ray Spectroscopy
FTIR	Fourier-transform Infrared Spectroscopy
HA	Hydroxyapatite
SDS	Sodium Dodecyl Sulphate
SEM	Scanning Electron Microscopy
SLA	Stereolithography
TCP	Tricalcium Phosphate
TGA	Thermogravimetric Analysis
UV	Ultraviolet
XRD	X-ray Diffraction

Chapter 1

Introduction

1.1 Contextualization

Since a very reduced number of people die as a direct consequence of bone diseases, the attention given to these disorders is underestimated when compared with other major conditions like heart issues or cancer. However, due to overall increase in life expectancy [1], it affects a large group of people and being capable of triggering a general downward spiral on a person's overall well-being and life quality, the lack of bone health is a critical public health topic [2].

Even though the therapeutical advances for bone diseases have been evolving, many others that lead to bone tissue loss, especially in localized areas, consist in a major clinical problem in reconstructive surgery [2, 3], particularly when the defect size prevents the natural repair mechanism [3, 4, 5].

Presently, the golden standard for osteogenic bone replacement is autologous bone grafting in which bone from a patient unaffected location is applied on the defect to stimulate bone formation. Grafts should allow the bone deposition and favor the surrounding bone integration and therefore, be osteoconductive. Furthermore, these grafts must be osteoinductive to promote the proliferation and differentiation of cells. Finally, as provider of stem cells and progenitor cells with the ability to form new bone, grafts should be osteogenic [3, 5].

Bone grafting based treatments are being used since the early 1900s [6] and, currently, over two million bone grafting procedures are performed every year, worldwide [7]. As proof, in 2005, in the United States alone, 500 000 bone graft procedures were performed with an associated cost of \$2.5 billion [8]. In fact, bone is the second most frequently transplanted tissue, being only surpassed by blood [9]. Some of the most relevant global bone grafting applications along with their respective share are presented in Figure 1.1.

Although this therapy has already achieved good results, some major limitations also exist. Besides the obvious limited tissue availability, it is difficult to apply in the treatment of irregular and geometrical complex bone defects and there is the need of a second procedure to harvest the tissue, enhancing the risk of morbidity at the donor site and surgical complications [11]. Some of the complications associated with this approach are listed on Table 1.1.

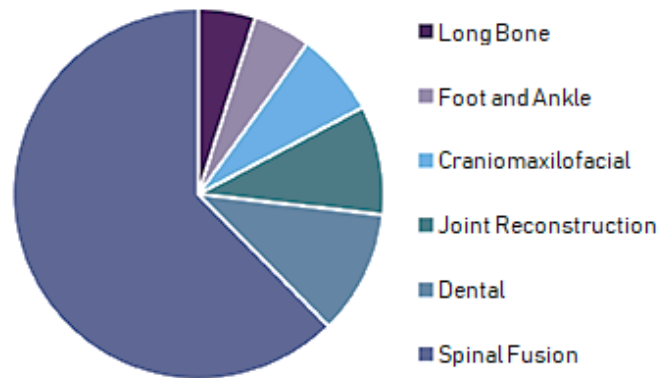


Figure 1.1: Global bone grafts market share, 2016. From [10].

Table 1.1: Classification of bone graft donor site complications. Adapted from [6].

Early complications	Late complications
Major	Major
Deep infection	Sensory loss
Prolonged wound drainage	Chronic severe pain
Large hematoma	Chronic infection
Reoperation	Large bony defect
Minor	Minor
Hematoma	Chronic mild pain
Wound drainage	Superficial infection
Severe pain	Delayed wound healing
Temporary sensory loss	Minor wound problems

Notwithstanding the major problems associated with autologous bone grafts, allografts and xenografts do not stand out as an appropriate alternative either. Allografts are implantable human bone tissues that are harvested from an external donor, living or cadaveric. In this way, there is an associated risk of viral diseases and bacterial contamination transmission [12]. Xenografts consist of bone tissue collected from an organism of a different species. Thus, even though the supply of available material is apparently endless, the possible transmission of zoonotic diseases and the recipients' immune response narrows this method's potential [12, 13]. Apart from the described technical difficulties associated with these alternatives, rises an even bigger issue: religious, moral and ethical concerns. The refusal rate associated to these grafts among the patients is relatively high due to the personal identity and integrity questions that must be considered when applying a bone substitution procedure [13, 14, 15].

Hence, it is necessary to establish new techniques and, as a consequence, the possibility to combine the advantages of autologous bone transplants with a reduction of secondary operations for tissue harvesting emerges: bone tissue engineering, regarded as any attempt to stimulate bone

formation with implants designed considering the principles of life sciences and engineering [3, 5].

The matrix-based bone therapy concept relies on the development of implants that, most closely, replace missing bony structures and facilitate healing.

Ideally, the implanted scaffolds should be designed to match to perfection the mechanical properties of the bone to replace. As some crucial requirements, the ideal scaffold must be biocompatible, biodegradable, osteoconductive, radiolucent to facilitate radiographical monitoring after implantation, easy to manufacture and sterilize and easy to handle in an operating room [3].

Since the main function of the scaffold is to support bone growth, the most critical step, when applying this therapy, is the matrix design, due to the importance of the three-dimensional microarchitecture for the promotion of cell ingrowth and cell distribution through the matrix [3].

Structures with a high composition of interconnected pores and with a large surface-to-volume ratio have the best osteoconductivity properties due to the high rates of oxygen, nutrients and metabolic by products mass transfer. The pore size is definitely one of the most crucial features when designing the matrix for bone regeneration; scaffolds with pore sizes between 200 and 900 μm have demonstrated to be the most suitable to the applications [3]. Scaffolds in which the pore geometry, with pore sizes of 150 μm and lower, restricts vascular ingrowth, do not support vascularization and promote the production of cartilage instead of bone, while scaffolds with large dimension porous will compromise the stability of the structure [3].

Another key aspect to consider, when developing an implant for bone tissue engineering, is the material choice. Permanent implant materials, like titanium or stainless steel, are not the best option for these applications as the bone tissue regeneration and remodeling is greatly dependent of mechanical stimulation that is absorbed, almost in its totality by the implant, causing a stress shielding effect and leading to bone resorption around the implant. Apart from that, these implants are also associated with infection, corrosion, fatigue and failure, requiring the recurrent replacement of the implant [5].

The scaffolds should be degradable by cellular enzymes, being gradually replaced by natural bone tissue. However, they must be able to prevail long enough so that the target cells can lay on the surface and produce extracellular matrix. The scaffold's premature degradation will negatively influence the volume of regenerated tissue, while the scaffold persistence will inhibit the development of the tissue [3].

1.2 Motivation and objective

Due to the increase life expectancy it is expected that, progressively and until the year 2020, the worldwide marketplace value of synthetic bone grafts will reach \$2.7 billion.

However, more complex surgical treatments have been performed which demand for complex bone graft structures. Additive manufacture is undoubtedly the one that can offer more advantageous solutions, since it offers the possibility to prepare three dimensional complex scaffolds with completely free geometrical forms, which is the main objective of this dissertation.

Also of great importance, this project aims to respond to actual clinical needs, requested by the global market and one specific medical device company.

These novel products are tailorable to each customer's specific needs and able to overtake most, if not all, existing products in the current market since the majority of the purchasable options are offered in either a granular, powder and block form that clearly do not replicate the complex structure of the bone.

Therefore, this dissertation project combines the great demand for bone graft materials with the most updated technology, additive manufacturing, to mimic the bone's complex structure.

Digital light processing has been the additive manufacturing technology chosen for this project since it is a reliable low cost technique which has been used in several other engineering applications and allows the production of high resolution pieces.

Chapter 2

Background and literature review

2.1 The Bone

Along with cartilage, tendons and ligaments, the 213 bones of the human body make the skeletal system which is the structural matrix that provides the body its characteristic shape [16, 17, 18].

Being the principal calcified component of most vertebrates, the bone can be described as a living, dynamic and highly vascularized, specialized connective tissue capable of growing, adapting itself to mechanical stresses and with a unique self-repair capacity. [3, 17, 19]

2.1.1 Elementary Constituents of Bone

Structurally speaking the bone can be defined as a porous composite material constituted by a dense matrix where bone cells are embedded in [2, 17, 19, 20].

Even though their chemical composition is identical, two types of bone, both macroscopically and microscopically different, can be found within the skeleton: cortical bone and trabecular bone (Figure 2.1). The cortical bone, which comprises 80% of the skeleton total mass, covers the outer part of all the skeletal structures and, being compact and dense and having a high resistance to bending and torsion, has as main function the provision of protection and mechanical strength. In turn, trabecular bone, comprises the majority of the bone surface and is found in the bone inner portions. It is less dense and more elastic, contributing to mechanical support in particular bones such as the vertebrae, and has a dominant metabolic function, providing the initial supplies of minerals when the organism homeostasis is deregulated [20].

2.1.1.1 Matrix

By weight, the bone matrix is composed by approximately 35% of organic material and 65% of inorganic [17].

Regarding the organic material, responsible for the matrix flexible strength, it consists primarily of collagen fibers usually packed in bundles and proteoglycans. The collagen fibers account

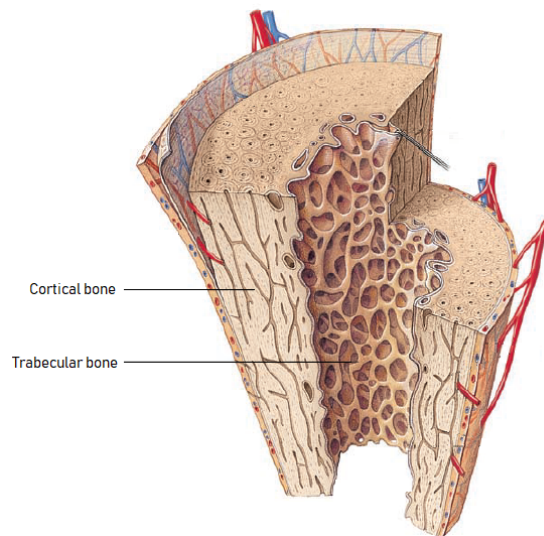


Figure 2.1: Representation of different bone types: cortical and trabecular. Adapted from [17].

for roughly a third of the bone matrix dry weight and their diameter is between 400 and 1200 Å [17, 19].

The inorganic component is mainly constituted by calcium phosphate crystals, usually referred simply as hydroxyapatite, granting the matrix compression strength. These crystals, tightly packed, present themselves in a needle-shaped or in a tabular form and can reach up to 600 Å in length.

The relationship between all the matrix components is extremely intimate one, with their integration approaching the molecular level [17, 19]. A matrix composed exclusively by inorganic material would be more brittle and break more easily. On the other hand, a structure made only of proteins would be soft and bend too easily [17].

2.1.1.2 Cells

Bone cells, having different functions and origins, can be classified as osteoblasts, osteocytes and osteoclasts [17].

Regarding the osteoblasts, they derive from osteochondral progenitor cells and present themselves as cells with a highly developed endoplasmic reticulum and numerous ribosomes. Organized in clusters and assuming a variety of shapes, their main function is to promote the ossification or osteogenesis [17, 19, 20]. In this way, they produce collagen and proteoglycans that are released from the cell by exocytosis. Additionally to the organic material production, osteoblast also promote the formation of hydroxyapatite crystals through the delivery of vesicles that accumulate calcium and phosphate ions. The matrix, newly synthesized by the osteoblasts, will cover the old bone and surround the osteoblast cells bodies and their processes [17].

When the osteoblast cell is completely trapped in the osteoid, it is classified as mature cell, an osteocyte [17]. Their activity and morphology modifies according to cell age; an older osteocyte accumulates glycogen in the cytoplasm and loses cell volume [20]. Even though the osteocytes are

relatively metabolic inactive cells, they remain capable to produce the necessary components to the bone matrix maintenance. The nutrients and gases distribution through the mineralized matrix is granted by the small amount of liquid that surround the cells or by gap junctions between the cell processes [17].

Lastly, the osteoclasts, large multinucleated cells derived from red bone marrow stem cells, are responsible for the bone resorption, presenting a ruffled border where their membrane contacts with the bone matrix [17]. These highly mobile cells present Golgi complexes, mitochondria and lysosomal enzymes loaded vesicles in a large number [19, 20].

2.1.2 Functions

The bone's importance to the normal functioning of an organism is undeniable, with its multiple functions being distributed throughout a broad spectrum of categories.

The bone, strong and rigid, being well adapted to load bearing, provides structural support to the body and is also the main responsible for the protection of vital organs and internal structures. Allowing the insertion of muscles, through the tendons, the bone plays a vital role towards the general locomotion since it is the main responder to the muscles contraction. In addition, besides working as a natural reservoir for growth factors, cytokines and some minerals, maintaining the mineral homeostasis and acid-base balance, the bone is also responsible for storing energy such as lipids in adipose cells of the yellow marrow. At last, the bone supports the blood cell production since it provides conditions within the red bone marrow filled cavities for hematopoiesis [17, 18].

2.1.3 Bone Remodeling

Bone remodeling is the process from which compromised old bone tissue is replaced for new bone to maintain mineral homeostasis and prevent the microdamage accumulation in the tissue, preserving the bone mechanical strength [17, 18, 21]. This process starts at birth and runs until death, with a slight increase of intensity in perimenopausal and early postmenopausal women and in aging men, and it is controlled by local and systemic factors to guarantee the fulfillment of structural and metabolic functions [2, 18].

Even though both processes, bone modeling and bone remodeling, work in harmony towards the skeleton benefit, it is important to clarify their differences [21]. While the first, highly active during childhood and adolescence, has as purpose the alteration of the spatial distribution of growing tissue involving either resorption or formation, the remodeling process combines the removal of mineralized bone by osteoclasts and the subsequent deposition of new matrix formed by osteoblasts [2, 20, 21].

The remodeling turnover of cortical bone is between 2 and 5% each year. The trabecular bone, having a more important role to mineral metabolism and having a substantial larger surface to volume ratio, is remodeled in a more active way [18, 20].

The bone remodeling sites are usually developed randomly but may also be targeted to reparation needing places by microcracks formation or osteocyte apoptosis.

The remodeling cycle comprises four phases (Figure 2.2): activation, resorption, reversal and formation [18]. Furthermore, it relies on a temporary anatomic structure, the basic multicellular unit (BMU), constituted by osteoclasts and osteoblasts, that mediates all the process, linking the cells behavior to the final bone form [21].

Some relevant statistical information on bone remodeling and, particularly, on the BMU can be found on Table 2.1.

Table 2.1: Vital statistics of adult bone remodeling. From [22].

Lifespan of BMU \sim 6-9 months
Speed \sim 25 $\mu\text{m}/\text{day}$
Bone volume replaced by a single BMU \sim 0.025 mm^3
Lifespan of osteoclasts \sim 2 weeks
Lifespan of osteoblasts (active) \sim 3 months
Interval between successive remodeling events at the same location \sim 2-5 years
Rate of turnover of whole skeleton \sim 10% per year

During the activation period, circulating mononuclear monocyte-macrophage osteoclast precursors are recruited and activated, the endosteum containing the bone surface lining cells is lifted and the formation of multinucleated preosteoclasts, by the fusion of multiple mononuclear cells, takes place. Through the interaction between integrin receptors in their cell membrane and Arg-Gly-Asp (RGD) containing peptides in matrix proteins, the preosteoclasts bind to the bone, forming, underneath them, sealed compartments [18].

The end of the activation phase sets off the resorption, with an approximate duration of two to four weeks. To favor the mobilization of bone mineral, the pH, within the sealed compartments, is lowered to levels as low as 4.5 as result of the resorbing osteoclasts activity: secretion of hydrogen ions through proton pumps and chloride channels in their membranes. To digest the organic matrix, osteoclasts secrete tartare-resistant acid phosphatase, cathepsin K, matrix metalloproteinase 9 and gelatinase, previously stored in cytoplasmic lysosomes, creating tunnel like cavities with an approximate diameter of 200 to 300 μm . After the multinucleated osteoclasts undergo apoptosis, the resorption finalization falls back to the mononuclear cells responsibility [18, 21].

The reversal stage consists in the transition from bone resorption to bone formation. By this time, the formed cavities accommodate a large set of mononuclear cells, including monocytes, osteocytes released from the bone matrix and recruited preosteoblasts for bone formation [18].

Finally, during formation, by the release of calcium and phosphate containing vesicles and the enzymatical destruction of mineralization inhibitors, osteoblasts synthetize a new collagenous organic matrix and, by the time they are surrounded or buried within matrix, turn into osteocytes. These are surrounded by a complex canalicular network that links them to bone surface lining cells, osteoblasts and other osteocytes. This remodeling stage lasts for four to six months and, by the time it is over, 50 to 70% of osteoblasts undergo apoptosis, having the remaining cells turned into osteocytes or bone lining cells. The latter, retaining the ability to redifferentiate into

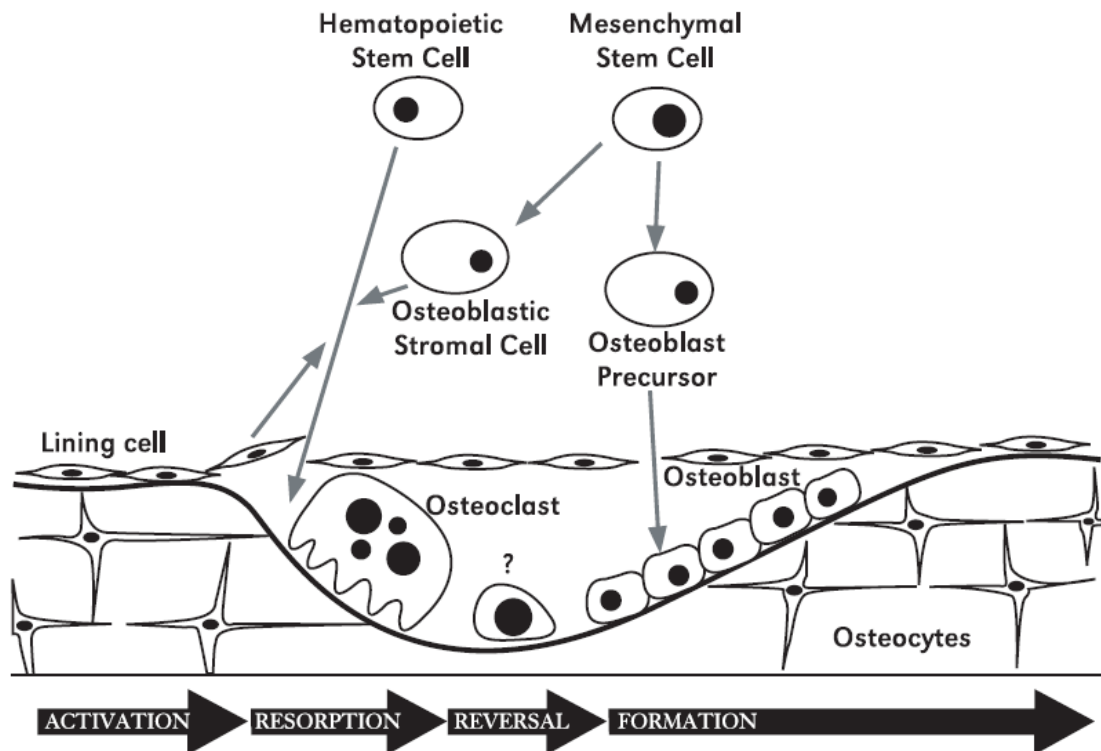


Figure 2.2: The bone remodeling sequence. From [2].

osteoblasts upon stimulation, serve as a blood-bone barrier, regulating the influx and efflux of mineral ions in and out the bone extracellular fluid [18].

Bone remodeling is highly conditioned by the level of mechanical loading. Shortage of loading accelerates bone resorption in comparison with bone formation, inducing a rapid bone mass loss. In turn, bone overuse may damage the tissue, stimulating overall bone remodeling [20].

As mention above, one of the possible triggers responsible for inducing bone remodeling is the existence of microdamage. These results of everyday life activities that expose the bone to cyclic forces, forging microscopic cracks that, with continued loading, enlarge, forming eventually, macrocracks. However, since the remodeling is associated to a transient increase in porosity and therefor, to a reduction of bone strength, the process itself is responsible to create further damage, playing, in this way, an important part in fatigue fractures [21].

2.1.4 Bone Health

Between common and not so common, and with multiple causes, the disorders that affect bone health are countless. Some of the most relevant ones will be described below.

Genetic and development disorders can play a major role in producing abnormal bones. Osteogenesis imperfecta, caused by collagen irregularities, leads to bone matrix weakening and favors the multiple fracture occurrence. In contrast, osteopetrosis, another congenital disorder, characterizes itself for the failure of osteoclast formation or function, resulting in bones too dense. Another

condition that affects bone health as a consequence of genetic factors but also in combination with environmental factors, possibly virus infections, is Paget's disease. It is marked by the formation of highly active and unregulated osteoclasts that trigger an abnormal bone resorption which is met by a compensatory increase of osteoblast activity to repair the damage. However, due to the architecture disruption, the new bone formed is disordered and bulky and might not be on the right place to maintain the expectable bone strength [2, 23].

The skeleton can also be affected by hormonal disorders. Hyperparathyroidism (overactive parathyroid glands) can cause excessive bone breakdown, fragilizing the bone, and, in extreme cases, large holes or cystic lesions may appear: osteitis fibrosa cystica. Hypogonadism (loss of gonadal function) may weaken the bone due to testosterone and estrogen deficit. Over production of cortisol by the adrenal gland can, eventually, lead to Cushing's syndrome, also with a negative impact in bone strength. At last, the use of glucocorticoids as a hormonal medication will cease bone growth in children and thin the bones in adults [2].

Another known cause for bone health impairment is nutritional deficits. The particular lack of vitamin D, calcium and phosphorus can be responsible for the formation of poorly mineralized weak bone [2].

Bacterial infections may also be responsible for damaging the bone through the direct effect of bacterial products or the production of local resorbing factors by white cells around the site of infection. This condition, osteomyelitis, can be caused, for example, by the entrance of *Staphylococcus aureus* into the organism through open wounds or by the *Mycobacterium tuberculosis* propagation from a primary infection site such as the lungs [2, 17].

Also, cancer, both solid tumors and hematopoietic disorders, can have harmful interactions with the skeleton since, by manipulating osteoclast formation and activity, it destroys bone tissue in order to establish itself and grow as metastases. The subsequent therapy itself may require even more bone tissue removal to resect the tumor's totality [3, 23].

In addition, some metabolic demands, such as high calcium needs that are necessary, for example, during pregnancy may weaken and soften the bones as result of the calcium depletion in the bone. This condition is called osteomalacia and it is a good example to illustrate why the bone health is difficult to preserve. The skeleton serves, simultaneously, two different functions that compete with each other. While it is responsible for weight bearing, requiring strong bones with large supplies of calcium and phosphorus, it also works as a storehouse for these two elements that, when in need to serve other systems, are withdrawn, leaving the bone weakened [2, 17].

Obviously, apart from the aforesaid conditions, trauma, fractures, possible improper fracture fixation and the well know osteoporosis also contribute for the general bone loss. To note that for every 10% of bone mass that is lost, the risk of further fracture doubles [3, 23].

2.2 Porous ceramics

The term ceramic derives from the Greek word *keramikos*, which means "burnt stuff", illustrating that these materials requested properties arise only after a high-temperature heat treatment: firing.

With a very complex crystal structure, the atomic bonding within these materials ranges from purely ionic to as far as totally covalent. However, most of the ceramics display a combination of these two bonding types; being the extent of the ionic character dependent on the electronegativity of the atoms [24].

Pores, contrary to the ones in polymeric materials, were once avoided in ceramic components due to their associated brittle nature [25]. In fact, any porosity will have a massive influence in both strength and elastic properties of the material; besides reducing the cross-sectional area crosswise the load application, they act as stress concentrators, amplifying the applied tensile stress. A 10% content in porosity may be able to cutdown the flexural strength up to 50% from the bulk material value [24].

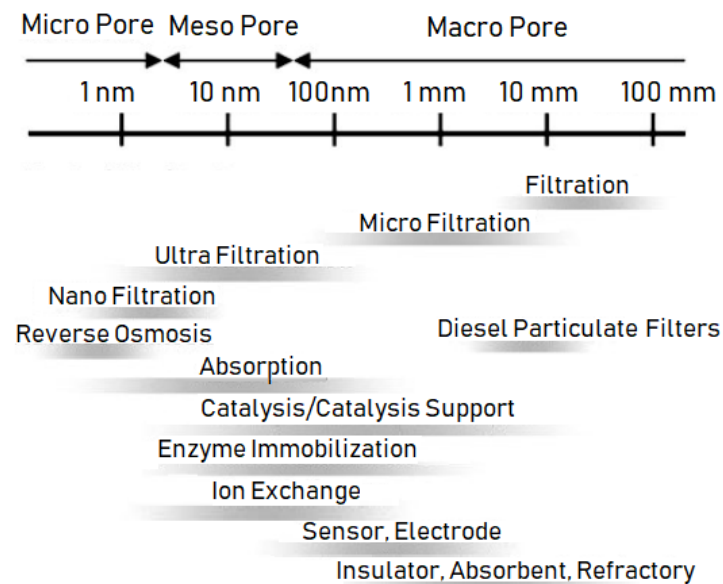


Figure 2.3: Correspondence between ceramic pore size and applications. Adapted from [26].

Yet, a growing group of applications that require porous ceramics have emerged in the past decades. See Figure 2.3. These materials are particularly relevant for harsh environments where high temperatures, considerable wear and corrosive media are involved due to their high melting point, tailored electronic properties, high corrosion and wear resistance. Additionally to these properties, some of the most attractive porous ceramics' characteristics are low thermal conductivity, controlled permeability, high surface area, low density and high specific strength [25]. All these properties can be tailored, having the ability to change the material's properties and functions to fulfill each unique application requirements [25, 26]. Due to the ceramics' great potential, many efforts have already been devoted to the previously mentioned tailoring and, as a result, a broad range of applications are currently at use [26].

2.2.1 Porous ceramics processing methods

The processing routes for porous ceramics, can be roughly classified into the following methods, schematically presented in Figure 2.4: partial sintering, replica, sacrificial template, direct foaming and solid-free forming [16, 26].

The partial sintering method is, probably, the most straightforward processing route for microporous scaffolds and it is performed using lower sintering temperatures and for a shorter time than the appropriate to obtain dense materials. Starting with porous powder compacts, the pore size and porosity is controlled by the initial particle size of the raw material and the degree of partial sintering. Porosities over 50% and with full interconnectivity are very difficult to obtain. The ceramic powder can be supplemented with pore forming agents to raise the porosity ratio and the pore size [16, 27].

Regarding the replica method, it is a processing route that relies on impregnation of a porous polymeric sponge or a natural cellular structure with a ceramic suspension; some of the possible replica templates are polymeric and carbon foams. The structure, that results after sintering, exhibits the same morphology as the original model; however, some of the porous interconnectivity is lost and, even though, the porosity ratio can reach high values, the material has low mechanical performances [25, 27].

The use of a sacrificial template to produce porous ceramics, unlike the replica method, results on a ceramic structure that is a negative replica of the original template. Porosity levels up to 90% can be reached when this method is used and the average pore size ranges from 1 to 700 μm . A composite is produced comprising a continuous matrix of ceramic particles or ceramic precursors and a sacrificial phase homogeneously distributed in matrix that, after extraction, will originate the pores. A broad range of materials has been used as pore formers and, the ones that are synthetic or natural are usually extracted resorting to pyrolysis, long thermic treatments at temperatures between 200 and 600 $^{\circ}\text{C}$; the burnout rate, however, must be limited to 20 mg/min in order to avoid cracking specially in thin ceramics. Mismatches in the thermal expansion coefficient between the organic and inorganic phases can also induce cracks within the porous structure during pyrolysis. Some sacrificial materials can also be extracted by chemical means. Apart from the chosen sacrificial template extraction technique, the continuous matrix must have to be already partially consolidated so that the porous structure does not collapse during extraction. When using pre-ceramic precursors, the consolidation is frequently achieved through a cure process that takes place at a slightly lower temperature than the one used in the pyrolysis step which allows the cross-linking of the molecules. Although it is a long process that may produce extensive amounts of gaseous by-products, it is a very simple process, flexible in the possible chemical compositions and it allows tailoring of porosity, size distribution and pore morphology. Furthermore, since the obtained scaffold is a negative of the original template, the extraction of the sacrificial material does not lead to structure flaws [16, 25].

Concerning the direct foaming technique, a cheap and environmentally-friendly method, it consists in the incorporation of a gaseous phase in a ceramic suspension or liquid. In order to fixate

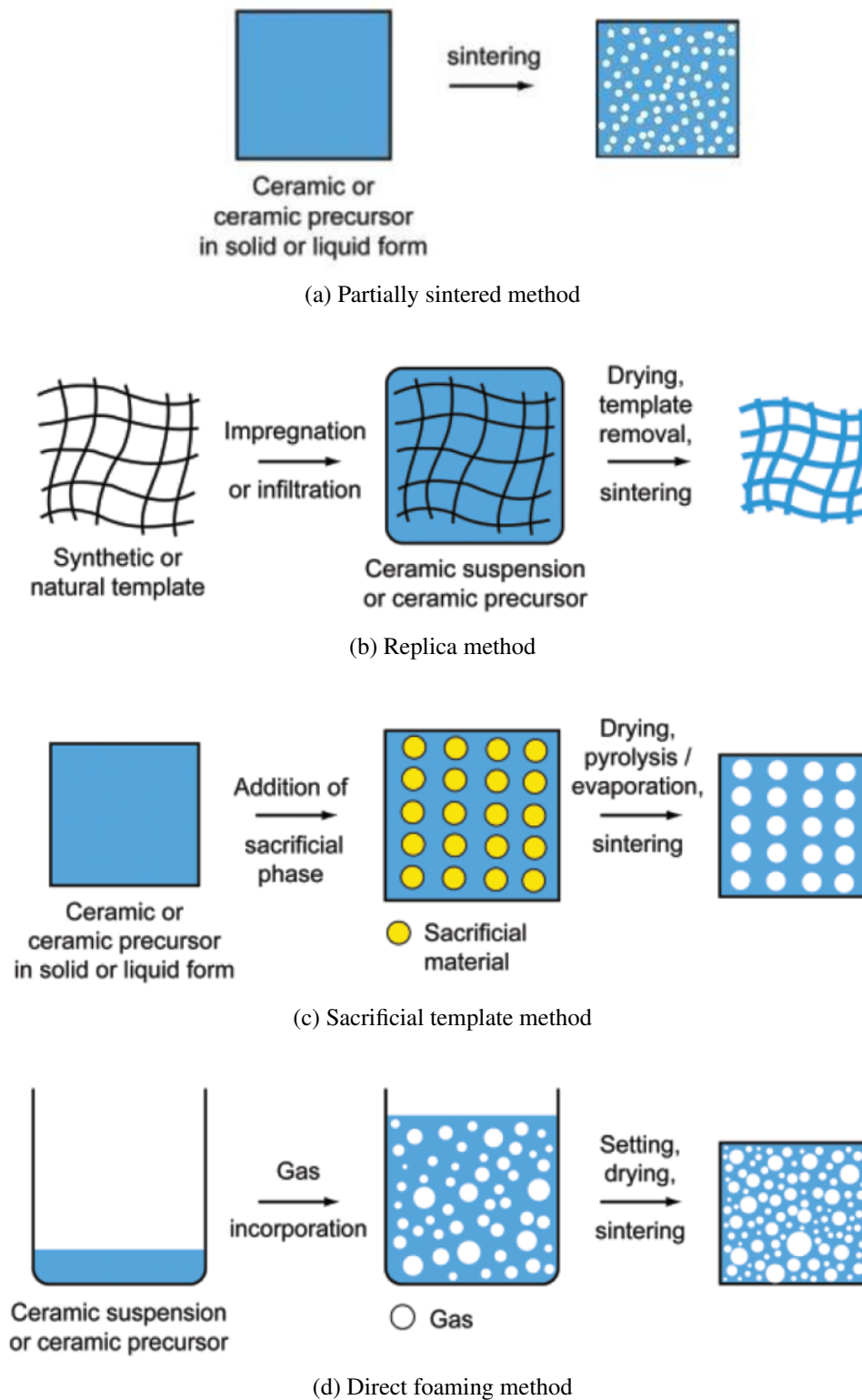


Figure 2.4: Possible processing routes used for the production of porous ceramics. From [25].

the air bubbles, the structure can be stabilized with surfactants and surface modified particles. The total porosity is proportional to the amount of the gas incorporated in the suspension with

porosities ratios of 45 to 95% [16, 25, 27].

Even though the above mentioned techniques do allow the creation of pore interconnectivity, it is not an intentional result of an *a priori* global design. In fact, the achieved connectivity is a product of random variable and local interconnections, affected by the processing parameters [16].

Finally, as a contrasting production method, solid-free forming, or rapid prototyping, concerns a variety of technologies, recently developed, that are able to produce complex physical constructs directly from computer-aided designs (CAD) adding material layer by layer [28]. These methods can produce directly the mentioned constructed but also a polymeric mold, shaped by rapid prototyping in which the ceramic slurry is poured [16].

2.2.2 Porous ceramics as bone substitutes

Recently a novel field of interest for porous ceramics has attracted great attention: tissue engineering and, in particular, bio-implants for bone regeneration [26].

When designing a sustainable ceramic scaffold with bone ingrowth as goal, it is necessary to establish a significant open and entirely interconnected pore structure, in order to allow the flow of cells and nutrients and provide space to cell attachment and proliferation. While the key importance of the tailored macroporosity is already well established, it is to note that the material's inherent microporosity is also biological relevant: cells migrate through the macropores as a result of the emission of long cytoplasmic extensions that are able to hang onto the microporosity on the surface of the structure [16].

2.2.2.1 Calcium phosphates

The mineral phase accounts for the great majority of the bone's total weight and most of it is in the natural hydroxyapatite form. With this in mind, it is intuitive that the development of synthetic substitutes will fall on the exploration of synthetic hydroxyapatite and other calcium phosphates [29] that can be part of the remodeling cycle. The optimal Ca/P ratios of materials for tissue engineering applications lie between 1 and 2 [16]. Table 2.2 presents some of the calcium phosphates that comply with this specific condition.

Hydroxyapatite (HA)

Due to its great chemical similarity to the mineral component of the bone, HA presents an immense potential for bone grafting and tissue engineering due to its biocompatibility with hard tissue along with skin and muscle tissues [16]. Synthetic hydroxyapatite is stoichiometric with a chemical formula of $\text{Ca}_{10}(\text{PO}_4)_6(\text{OH})_2$ and highly crystalline, displaying hexagonal symmetry. Its crystals usually present themselves in a needle-like morphology [31].

It is the most stable calcium phosphate salt at normal temperatures and pH between 4 and 12 and, therefore, HA-based biomaterials have been, until now, the most used materials in normal bone substitution applications as non-load bearing implants and as coatings on metal implants for load bearing [32, 33, 34].

Table 2.2: Several calcium phosphates and their respective Ca/P atomic ratios. From [30].

Ca/P atomic ratio	Name	Formula	Acronym
2.0	Tetracalcium phosphate	$\text{Ca}_4\text{O}(\text{PO}_4)_2$	TetCP
1.67	Hydroxyapatite	$\text{Ca}_{10}(\text{PO}_4)_6(\text{OH})_2$	HA
1.50	Tricalcium phosphate	$\text{Ca}_3(\text{PO}_4)_2$	TCP
1.33	Octacalcium phosphate	$\text{Ca}_8\text{H}_2(\text{PO}_4)_6 \cdot 5\text{H}_2\text{O}$	OCP
1.0	Dicalcium phosphate dihydrate	$\text{CaHPO}_4 \cdot 2\text{H}_2\text{O}$	DCPD
1.0	Dicalcium phosphate	CaHPO_4	DCPA
1.0	Calcium pyrophosphate	$\text{Ca}_2\text{P}_2\text{O}_7$	CPP
1.0	Calcium pyrophosphate dihydrate	$\text{Ca}_2\text{P}_2\text{O}_7 \cdot 2\text{H}_2\text{O}$	CPPD
0.7	Heptacalcium phosphate	$\text{Ca}_7(\text{P}_5\text{O}_{16})_2$	HCP
0.67	Tetracalcium dihydrogen phosphate	$\text{Ca}_4\text{H}_2\text{P}_6\text{O}_{20}$	THDHP
0.5	Monocalcium phosphate monohydrate	$\text{Ca}(\text{H}_2\text{PO}_4)_2 \cdot \text{H}_2\text{O}$	MCPM
0.5	Calcium metaphosphate	$\text{Ca}(\text{PO}_3)_2$	CMP

Since its first use as a biomaterial, various are the clinical applications of synthetic hydroxyapatite scaffolds as bone graft substitutes. The two major areas that rely on the use of HA scaffolds as a tissue engineering tool are the dental and orthopedic fields. The main clinical uses of these scaffolds, in orthopedic surgery, are reparation of bone cranial and maxillofacial defects, obliteration of cystic cavities, filling of mandibular and facial bone osteotomy, treatment of benign bone tumors and in periorbital interventions. Apart from these two major classes, hydroxyapatite scaffolds are also successfully applied in spinal fusion surgery to aid the fusion of adjacent vertebrae and as ocular implants [16].

Apart from stand-alone implants, hydroxyapatite can be applied to metallic implants surface by plasma spraying. The main role of HA in this approach is to promote the fixation of the implant to the surrounding tissue. This strategy is currently used in hip, knee, ankle, hand, spine and dental implants [16]. Some of other interesting trend for HA applications comprise drug delivery, cell culture and purification of antibodies on industrial scale [31].

Tricalcium phosphate (TCP)

It can be found in two distinct crystallographic configurations: α -TCP, more soluble, and β -TCP, relatively more stable [29].

It has a shelf life of, at least, eight years, and, even though no osteoinductive activity has been reported, there are clear indications that allow the TCP characterization as osteoconductive, providing a scaffold for vascular ingrowth and new bone formation [35].

Its biodegradation rate is higher than the one of HA and, while most of the TCP scaffold is resorbed within the first months, some material remains for longer periods being incorporated in the new structure without disturbing the blood natural levels of calcium and phosphorus [29, 35]

Currently, some of the applications that rely on TCP are used in dental repair, in particular as a filling in periodontal osseous lesions [29]. Also, good results have been reported when using tricalcium phosphate scaffolds to repair avulsive wounds and orofacial fractures [35]. TCP also

shows promising properties in promoting bone formation and fixation when coating hip prostheses [32].

2.3 Modelling and Three Dimensional Printing

Modeling, either numerical or physical, is without doubt a very useful tool for engineers and scientists, allowing them to clarify physical phenomena, to evaluate physical objects and systems and to design [36].

Furthermore, the development of three dimensional (3D) printing technologies, also known by additive manufacturing (AM), that unlocked advanced and efficient production processes is now allowing the accurate production of physical models with big levels of intricacy [36].

Design engineering, manufacturing and marketing are some of the areas that benefit from these types of techniques since they facilitate the visualization of conceptual models and, therefore the design evaluation, verification and optimization, reduce the time to market (an important feature that defines a successful product introduction), produce prototypes (which can be used for reproducibility studies and speed up the process planning and tooling design) and assist product sales, demonstrating the design ideas and feasibility, the concept and the company's ability to produce it [37].

2.3.1 Three Dimensional Printing Techniques

According to the American Society for Testing and Materials, the approaches that allow the three dimensional construction of computer generated models can be sorted into seven distinct categories [38], schematically represented in Figure 2.5:

- **Binder Jetting**
The process resorts to two different materials: a powder based material and a binder, frequently in a liquid form [39]. The powder particules are binded together when the binder agent is selectively extrude by a print head [40]. After each layer, the build platform is lowered and it is spread another layer of powder [39].
- **Directed Energy Deposition**
This technique consists on a phased ejection of a material, usually a wire or a powder, onto a specific surface, The material melts upon deposition by the action of a highly powerful laser, creating each layer simultaneously with the solidification [39, 40].
- **Material Extrusion**
Usually, being applied to thermoplastic materials, this process consists in selectively dispensing the material that is pushed through a heating nozzle at constante pressure and continuous stream [39, 41]. The different layers are bonded by the control of the deposition temperature or by the use of chemical agents [39].

- Material Jetting

Through a moving nozzle and using either a thermal or a piezoelectric method, drops of materials are jetted onto the building platform in a comparable way to a two dimensional ink jet printer. After solidification of each layer, the material is generally photo-cured [39].

- Powder Bed Fusion

A powder bed is fused through thermal energy generated by a laser or electron beam. After each layer is fused, the building platform descends and another portion of powder is tilled over the top using a roller [41]. The post processing procedure removes loose and unfused powder [39].

- Sheet Lamination

Starting of with sheets or ribbons of material, each layer is placed on the cutting bed and cut to achieve the desired design using knives or lasers [39]. The piled layers are bond resorting to adhesive bonding, thermal bonding or clamping [40].

- Vat Photopolymerization

A photo curable resin is selectively polymerized through an energy source such as a laser beam or a projection system lamp. After each layer is cured, the building platform moves in order to expose a new portion of resin [41]. Since this technique resorts to liquid materials to create the final form, there is no structural support during the assembly and it may be necessary to add supports [39].

2.3.2 Biomodel

Obviously, also in the medical and bioengineering field, the current developments have a great impact and are used for a wide range of applications in particular for anatomical structures visualization, fundamental biomechanical processes investigations, design and prototyping of surgical implants and surgical training [36].

A definition from D'Urso *et al* and adapted by Lohfeld *et al* claims that a biomodel is an entity that replicates the geometry or morphology of a biological structure, which can be presented in either a computer-based form or a solid physical form [36, 42].

From this definition two distinct groups of biomodels arise. The first, computer-based biomodels, can be split into two different types: virtual biomodels and computational biomodels. Regarding virtual biomodels, their purpose is to allow the visualization of biological structures in a 3D format generated from computed tomography (CT) scans or any imaging technique that is able to continuously scan the target, that can be used for surgical planning, diagnostics or to design implants and prostheses. A computational biomodel is created to implement biomechanical analysis on biologic structures such as determination of stress and strain distributions and, therefore, the material properties of the structure to mimic play a role as important as the structure's geometry [36].

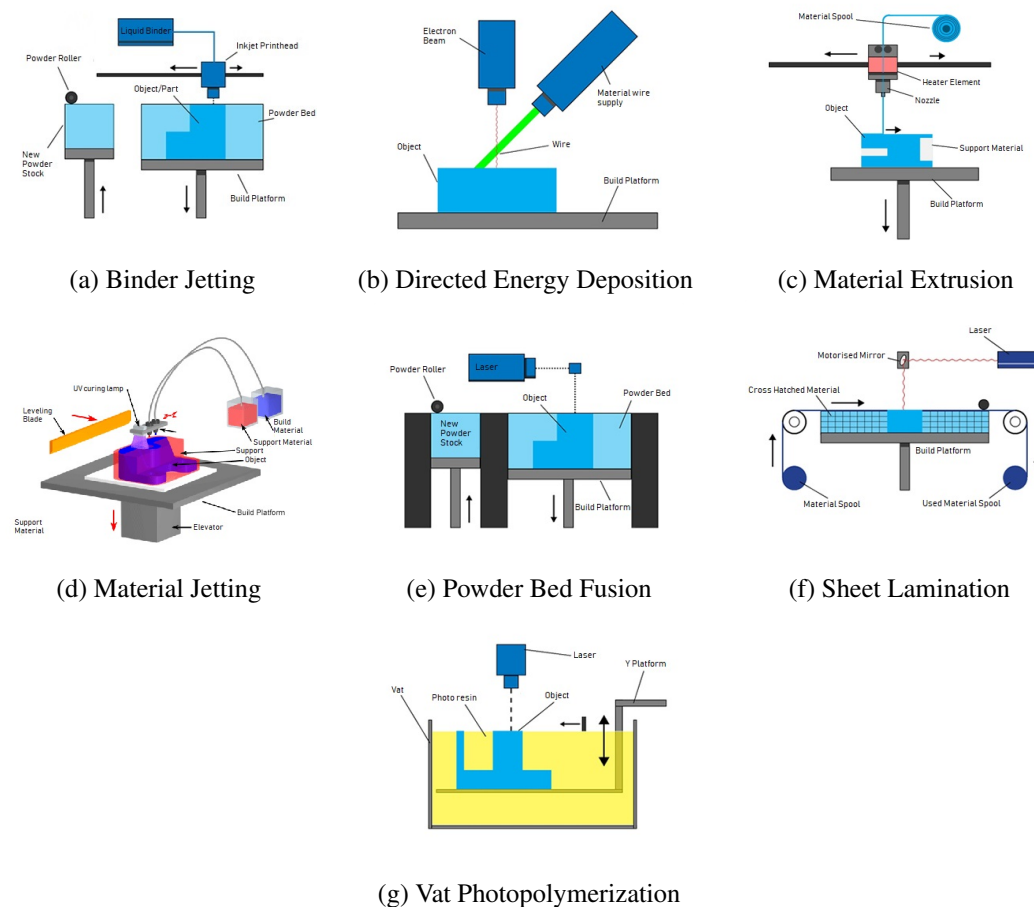


Figure 2.5: The seven categories of additive manufacturing processes. Adapted from [39].

The second group of biomodels comprises the physical biomodels: the solid representation of a computer-based biomodel, in particular, a virtual biomodel. These models, after designed by a CAD software, can be produced by engineering technologies such as the rapid prototyping techniques [36, 43]. Physical biomodels can be applied to the overall anatomy, including the cardiovascular and gastrointestinal systems and endocrinal organs [36].

2.3.3 Bone Applications

When referring to biomodels for bone applications, two different scales of organization arise: the macro and the micro scales [36]. See Figure 2.6.

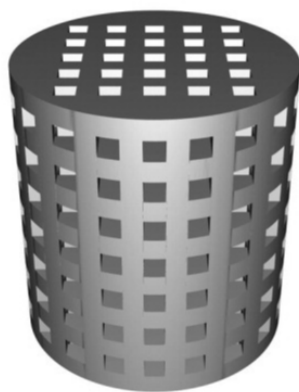
When producing bone biomodels at the macro scale, the focus falls on the bone as a whole structure. Geometric information is extracted from a series of two-dimensional scan images that are processed to eliminate the noise around the interest region. Their integration allows the stack of contours which can be computationally transformed into a three-dimensional triangle mesh model. The chosen format for the model can differ to meet the objective of the file. For visualization purposes only and not to preform simulations, a Standard Triangle Language (STL) format is

appropriate and can be applied to rapid prototyping that, layer-by-layer, produces the desired physical model [36, 44].

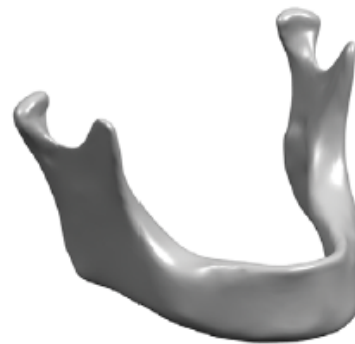
Virtual models at the macro scale are very useful for preoperative diagnosis and planning of surgical procedures, assessing the practicability of the planned surgical intervention and, therefore, reducing significantly the risk for the patient. They allow bone virtual manipulations, such as shape changings and risk of fracture estimations in a non-destructive way, facilitating the evaluation of multiple alternatives and combinations. In addition, these models, representing in the most reliable form the exact structure of the tissues, are very useful for the development and refinement of novel engineering systems for medicine like robots used for surgery. Finally, the digital information of the model can be used to boost the communication between surgeons worldwide, thus improving the overall quality and safety of intricate procedures, based on opinions from diverse highly qualified professionals [36].

The 3D physical models also play a vital role for medical education and training because they serve as tactile and visual support that, for example, allow the physician to have a “feel” about the bone thickness in order plan the procedure’s details such as resections and drillings [36].

Further, the sophisticated virtual model conversion into a physical model can be used to design the implantable structure which can have extremely complex geometries, mimicking the target bone. Customized prostheses have already been applied to dental and mandible restoration and hip, femoral and hemi-knee joint reconstruction [36, 44].



(a) Micro scale bone model. From [45].



(b) Macro scale bone model. Adapted from [46].

Figure 2.6: Examples of bone models.

Micro scale models contrast with the macro scale models since they represent structures with very reduced dimensions at the trabecular bone scale. Therefore, the imaging technique required to obtain the geometric information from the biologic tissue is Micro CT scanning [36].

Even though these models are very useful for flow studies, providing a better understanding of the underlying details of the physiological fluid passage through the trabecular bone microstructure, their most promising application is in the tissue engineering area. Micro scale bone models,

mimicking the biologic structures' geometry, can be used to replace bone defective regions and support or even promote bone growth. These models, replicating the mechanical properties of the trabecular bone, allow the impartial evaluation of the importance of an implant's geometry alone and their ability to guide tissue ingrowth [36].

For bone regeneration, highly porous structures are required and high levels of geometry complexity can be reached. In this way, computational modelling is a very efficient method to produce custom-made scaffolds since it allows the optimization of the scaffold's design and manual modifications in terms of porosity and shape, and, then, using rapid prototyping techniques, the solid model, which should resorb into the body simultaneously to the bone formation, can be produced from the computer-generated design [36, 44].

The rapid prototyping approaches to standard bone micro scale models creation can also be applied to the manufacture of scaffolds with live cells and tissues or with growth factors, thus improving the overall progress of bone defects reparation [47].

All the physical biomodels for biologic implantation have, as a production critical step, the material's choice since the prime goal is not visualization alone but also meeting the desired properties of the living tissue [36].

Chapter 3

Materials and Methods

3.1 3D Printer

Digital light processing (DLP), graphically represented in Figure 3.1, is a vat polymerization process that builds customized objects by curing selectively portions of a photosensitive resin in a layer-by-layer way [48] without the need of specialized expensive equipment such as lasers or heating chambers and with no environmental conditions restrictions [49].

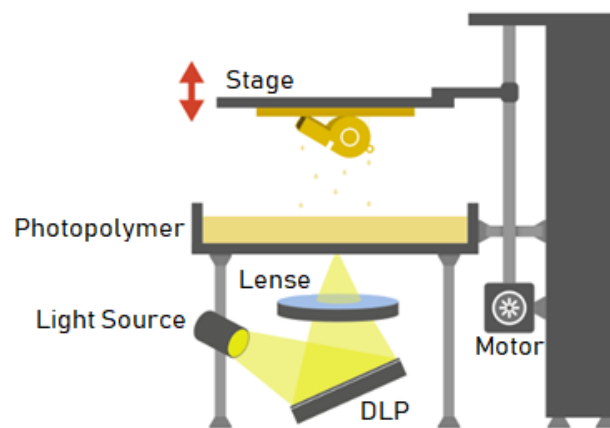


Figure 3.1: The working principle of DLP printing. From [50].

The “*digital light processing*” term refers to the method by which the photosensitive resin is selectively exposed to visible or ultraviolet light in order to promote the polymerization, either by the use of a set of micro mirrors that can be individually tilted in an on/off state or by the use of a liquid crystal display (LCD) screen. In both cases, a dynamic mask is created, projecting a two dimensional pattern on the surface [51].

The exposure to light will cause the polymeric resin to solidify at the desired area, while the non-exposed polymer remains liquid. After each layer is cured accordingly to desired pattern, the platform will move so that another layer of uncured liquid can be patterned [47, 52].

Being very similar with another vat polymerization process, stereolithography (SLA), DLP printing displays a major difference that is responsible for reducing significantly the printing times: the light source. Contrary to SLA printing that targets the light onto one single focal point, DLP resorts to a projector and cures an entire layer with a single exposition. In a cut down metaphore, it is “(...) *the difference between stamping and drawing an object*” [48].

A low-cost LCD DLP 3D printer, supplied by the partner company, was the equipment used to develop the work of this dissertation project. It is an easy to handle printer with an user friendly interface, accessed by a touch screen where the printing process is displayed in real-time. It is associated with its own open-source slicing software capable to process a 30-megabyte file within 1 minute which can be saved in a regular Universal Serial Bus (USB) stick and directly read by the printer that supports off-line printing. This software splits the model into layers of a designated thickness specified by the user and it has a straightforward handling, allowing the simple manipulation of printing variables. Furthermore, it offers the possibility to automatically generate all the supports needed so that the model can be successfully printed without structural failure. This innovating DLP printer uses an unique resin vat that increases largely the lifetime of the fluorinated ethylene propylene film that is an expensive consumable for 3D printings and facilitates its substitution. Moreover, this printer is equipped with an activated carbon air purification system that filtrates bad smells and keeps the air clean, promoting the user's safety.

3.2 Raw Materials

3.2.1 Resin

Since it is a fundamental component that highly influences the success of the 3D printing process, the choice of the resin to be used is extremely important. It was compulsory to use a resin that would allow the incorporation of solid powders while maintaining the essential physical-chemical characteristics for a DLP print.

The commercial product chosen was provided by the company. It is a photopolymer curable resin base suitable for DLP and SLA 3D printing described as "*a mixture of methacrylated monomers, methacrylated oligomers and a photo initiator*" that, together with solid powders creates a novel 3D print resin.

Some guidelines were provided, however, experimentation beyond them is encouraged. In some cases, as it happens in this project, the resin burn-out and/or sintering may be desired but the firing schedule is dependent upon the vitrification or sintering temperature of the material combined with the resin; nevertheless a slow heating ramp is recommended to avoid cracking.

3.2.2 Hydroxyapatite powders

Two different hydroxyapatite synthetic powders from distinct providers were used for the conduction of this dissertation project. For nomenclature proposes, from here on, these two powders will be denominated as HA1 and HA2.

3.3 Formulations

In order to prepare the printable suspensions, it was mandatory to define their constitution. It was decided to include a dispersing agent in the formulation in addition to the resin and the HA powder with the purpose of stabilizing the suspension and obtaining satisfactory rheological properties. An adequate surfactant may be able to promote the particle separation, avoiding their clumping and, in this way, plays a crucial role in the preparation of a suitable printable suspension with an high volume of loaded particles [53].

The preparation of stable ceramic slurries has been highly researched and, regarding hydroxyapatite suspensions specifically, it is reported that surfactants with an anionic character are the ones that better stabilize these particles [54, 55].

The selected dispersing agent, sodium dodecyl sulphate (SDS), is the most extensively adopted anionic surfactant, usually found under the powder form and has already been applied to stabilize hydroxyapatite suspensions [54, 56, 57]. SDS ($C_{12}H_{22}SO_4Na$), is composed by a 12 carbon tail that leads to a closing sulfate group which is responsible for the surfactant's amphiphilic properties; its molecular structure is represented in Figure 3.2 [56, 58].

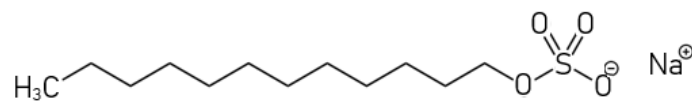


Figure 3.2: Molecular structure of sodium dodecyl sulphate.

Different suspensions, varying either the nature of used hydroxyapatite powder (HA1 or HA2) or the content of powder loaded, were formulated and their composition is discriminated in Table 3.1.

Three different HA loading levels were defined and are here designated as L1, L2 and L3. Sorting these loads by increasing HA concentration order, it comes as:

$$L1 < L2 < L3$$

Concerning the SDS incorporation, John W. Halloran *et al*, who developed a photo curable resin for use in rapid prototyping of ceramic or metal structures, reported the ideal range for dispersant incorporation in a ceramic suspension: 0,5 wt% to 5 wt% [53]. After some preliminary experiments, an invariable 2 wt% value for SDS incorporation was set.

The first stage of the suspensions' preparation is the combination of the two powders together. The hydroxyapatite powder and the surfactant are mixed in together for 30 minutes, following the above mentioned determined relative amounts, using a 3D shaker mixer: *TURBULA*® from *WAB* company. This equipment, due to its harmonic three-dimensional motion, effectively combines homogeneously the two powdery substances together, making them ready for incorporation within the resin.

Table 3.1: Composition discrimination of the different printable prepared suspensions.

Formulation	Composition			
	HA (w/v%)	HA powder	Dispersant (wt%)	Dispersant
1	L1	HA1	2	SDS
2	L2	HA1	2	SDS
3	L3	HA1	2	SDS
4	L1	HA2	2	SDS
5	L2	HA2	2	SDS
6	L3	HA2	2	SDS

This incorporation is executed through an incremental method by which the total powder is added to the resin's volume in four individual dosages. The amount of powder incorporated decreases with the sequential increments whereas the mixing time increases. Again, the equipment used was the *TURBULA*® and, to improve the efficacy of the method, grinding balls were placed inside the mixing container.

Finally, the suspension is then ready to be printed in order to create the desired 3D structure. It is important to highlight that, due to photo curable nature of the resin, the suspension's preparation must be, as far as possible, completed in a radiation protected environment to avoid undesired polymerization.

3.4 Material characterization

3.4.1 Raw Materials

3.4.1.1 Resin

Fourier-transform infrared spectroscopy (FTIR)

With the purpose of extracting qualitative chemical informations, after being polymerized through ultraviolet-light (UV) exposition, a resin sample was analyzed at *Instituto de Investigação e Inovação em Saúde* (i3S) using the *PerkinElmer Frontier FT-IR* spectrometer. The infrared spectrum was obtained with a 1 cm^{-1} resolution and 3601 scans were collected.

Thermogravimetric analysis (TGA)

Thermal analysis of the polymerized resin took place in *Departamento de Engenharia de Materiais e Cerâmica* (DEMaC) at *Universidade de Aveiro* with the intention of studying the sample's behaviour under a predetermined temperature profile.

The equipment used was *LabsysTM TG-DSC16* from *Setaram* and, during the data acquisition, temperatures ranged from 60 to 1300° with a scanning rate of $4^\circ\text{C}/\text{min}$ and under an oxygen flow.

Energy dispersive X-ray spectroscopy (EDS)

To identify the elemental composition of the non-organic residues, a block of polymerized resin

was submitted to a heating cycle up to 1300 °C for one hour with a 4 °C/min pace in order to achieve maximum burn-out of the organic phase. The resulting ashes were then characterized using energy dispersive X-ray spectroscopy to obtain a qualitative identification of the chemical composition of the sample.

The sample was analysed using *Quanta 400 FEG ESEM / EDAX Genesis X4M* at *Centro de Materiais da Universidade do Porto* (CEMUP) after being secured to the aluminum supports using carbon tape and submitted to a sputtering treatment to deposit a thin gold-palladium coat using the *SPI Module Sputter Coater* equipment with a 15 mA current during 80 seconds.

Viscosity determination

The determination of the resin's viscosity was carried out at *Departamento de Engenharia Química* at *Faculdade de Engenharia da Universidade do Porto* (FEUP), using the rotational rheometer *MCR92* from *Anton Paar* equipped with a plate system of 50 mm in diameter. The analysis was performed at 20 °C temperature and using a gap of 0.5 mm. For the data acquisition, the shear rate ranged between 1 and 100 Hz and the obtained curve was designed with 50 points.

3.4.1.2 Hydroxyapatite powders

Granulometric analysis

Rheometer Particle size distributions of the different hydroxyapatite powders was assessed through a granulometric analysis at *Departamento de Engenharia Química* at FEUP.

The used equipment was the *LS 13 320* particle sizing analyzer from *Beckman Coulter* and the size acquisition ranged from 0.040 to 2000 μm .

Scanning electron microscopy (SEM)

To discern the detailed superficial morphology of the particles, different hydroxyapatite powder samples were analyzed through scanning electron microscopy at CEMUP.

The samples were attached to the aluminum supports using carbon tape and then sputtered with a thin film of gold-palladium using the *SPI Module Sputter Coater* equipment with a 15 mA current for 80 seconds.

The analysis was performed resorting to *Quanta 400 FEG ESEM / EDAX Genesis X4M*: a high resolution (Schottky) environmental scanning electron microscope with X-ray microanalysis and electron backscattered diffraction analysis.

Zeta potential measurement

To determine each HA powder surface charge, a set of zeta potential determination analyses were executed at i3S.

The *Zetasizer Nano ZS* from *Malvern Instruments* equipped with a 4 mW HeNe laser beam with a wavelength of 633 nm and a scattering angle of 13 ° was the equipment used to perform the zeta potential measurements at 25 °C.

The hydroxyapatite powder samples were tested dispersed in distilled water at a 0.1 mg/mL concentration with a pH of 6.5 and in a *DTS1070* cell: a polycarbonate folded capillary cell incorporated with gold plated electrodes.

The analysis was rendered using the *Automode* model, having the voltage and the subrun number been automatically assigned by the software that, after measuring the electrophoretic mobility of the sample and using the Henry equation with the Smoluchowski approximation, calculates the zeta potential value as an average based on three individual measurements. The measurements were performed in triplicate and reported the mean values.

X-ray diffraction (XRD)

In order to evaluate the crystallinity of the hydroxyapatite powders, XRD analyses were carried out in *Serviços de Caracterização de Materiais* at *Universidade do Minho*. The XRD acquisition was performed in the $5\text{-}80^\circ 2\theta$ range with a 0.04° stepsize and an acquisition time corresponding to 1 second per step.

3.4.2 Processed materials

X-ray diffraction

To discern the possible crystallinity and thermal stability differences, after being compacted into cylindrical green bodies by uni-axial pressing, sintered to achieve maximum densification and then grinded to a fine powder, different HA powders were analysed as described in Section 3.4.1.2.

3.4.3 Produced samples

3.4.3.1 Formulations

Viscosity determination

To determine the ceramic loaded suspensions' viscosity, the same procedure that was applied to the resin, mentioned in section 3.4.1.1, was employed.

3.4.3.2 Printed pieces

Scanning electron microscopy

The SEM analysis was the chosen technique to investigate the samples' micro-structure and was performed at *Centro de Materiais da Universidade do Porto* resorting to *Quanta 400 FEG ESEM / EDAX Genesis X4M*: a high resolution (Schottky) environmental scanning electron microscope with X-ray microanalysis and electron backscattered diffraction analysis.

Porous samples (Figure 3.3) were mounted onto the aluminum supports using *Araldite*® glue and fixed with a carbon conductive adhesive tape while non-porous samples were directly secured to the supports using only the carbon tape.

By sputtering, both types of samples were coated with a thin gold-palladium film using the *SPI Module Sputter Coater* equipment with a 15 mA current, having the samples been submitted

to a 100 second treatment.



Figure 3.3: 3D porous sample prepared for scanning electron microscopy.

X-ray diffraction

In order to evaluate if the 3D printing and the postprocessing are responsible for any phase change of the used ceramic powder, after printing and firing procedure, the produced samples were grinded to a fine powder that was analysed by X-ray diffraction. The specifications of the XRD acquisition were the same applied to the HA powders alone and can be found on Section 3.4.1.2.

Linear and volumetric shrinkage assessment

The inherent ceramic shrinkage associated to the thermal treatment applied to the 3D printed pieces was experimentally evaluated by a simple comparison between the pre and post sintering dimensions of the pieces. The contraction value of each dimension (x, y or z) can then be easily calculated resorting to Equation 3.1.

$$Contraction(\%) = \frac{Initial\ dimension(cm) - Final\ dimension(cm)}{Initial\ dimension(cm)} \cdot 100 \quad (3.1)$$

Porosity determination

The total pore content of a printed piece was estimated by the following equation (3.2):

$$Pore\ content(\%) = \frac{Pore\ volume(cm^3)}{Geometric\ piece\ volume(cm^3)} \cdot 100 \quad (3.2)$$

To determine the pore volume, the mass of each 3D piece was divided by an estimated value of the density of the material, which was calculated using the fraction and the density of each pure phase.

Chapter 4

Modeling and 3D Printing

To successfully create the desired models for the 3D printing it was necessary to acquire some basic skills of 3D files manipulation. For this reason, the Modeling in Biomedical Engineering classes (Master in Bioengineering, *Faculdade de Engenharia da Universidade do Porto*) were attended.

All of the used models were derived from one single primary file: Figure 4.1. This virtual model was purchased online by the company and reproduces the characteristic patterned design of the trabecular bone geometry. It emulates its complex structure in a sphere form, maintaining the high surface area linked to the open porous framework, granting the typical spongy-like appearance.

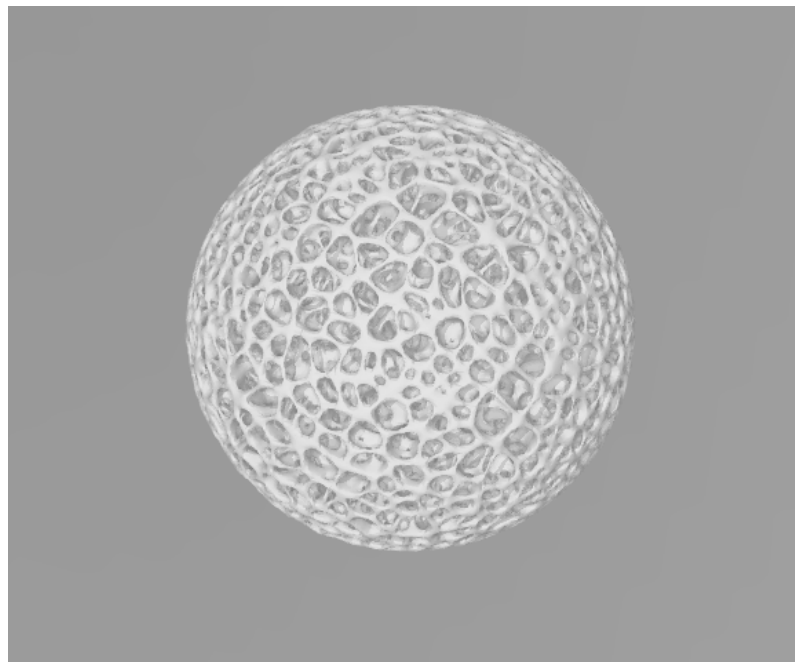


Figure 4.1: Original trabecular structure for model design: structural sphere.

From this structure and using the *3D Builder* software from *Microsoft®*, distinct models, with

different aims, were produced by applying a series of editing techniques to the original file in order to obtain different 3D structures after 3D printing. Some of these models are presented in Figure 4.2.

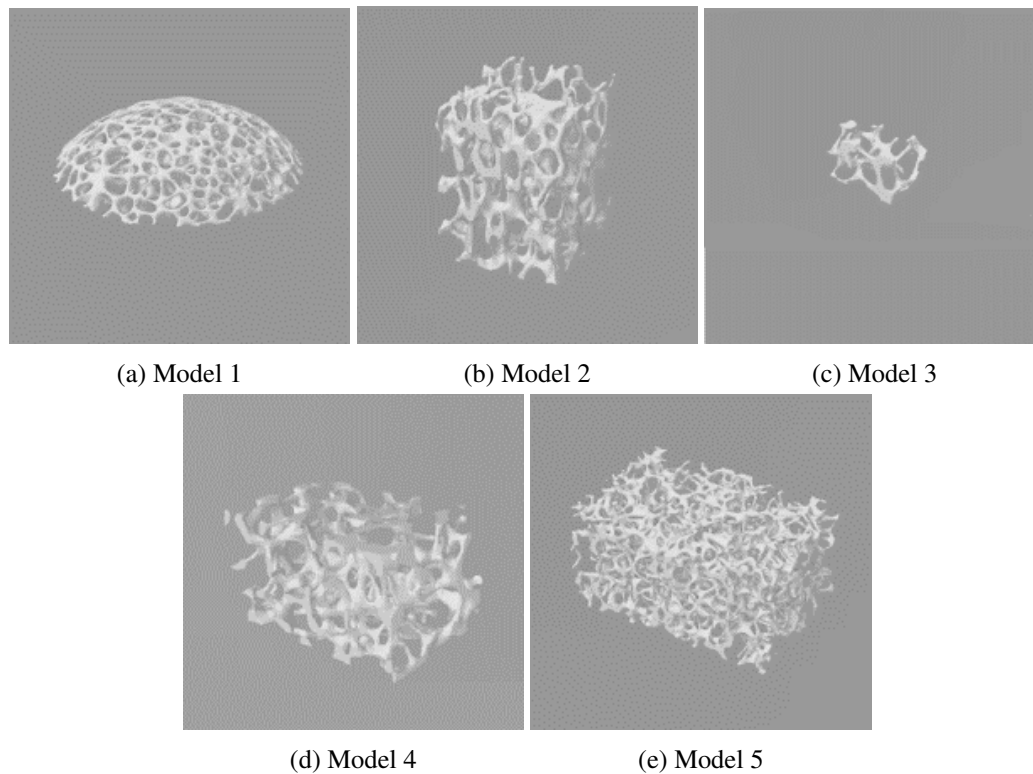


Figure 4.2: Different virtual models, originated from the same original file, used during the development of the project.

Model 1 (Figure 4.2a) was the first variation adapted from the original CAD design. It is the result of a straightforward manipulation of the original file as it simply consists in the top portion of the structural sphere. This model was created in order to preform the introductory studies and optimize the printing procedure.

As to Model 2 (Figure 4.2b), it was designed with the goal of producing pieces with a defined three axes system, under the form of a parallelepiped, to evaluate, as accurately as possible, the ceramic samples' shrinkage upon sintering.

Combining the intention of wisely managing the resources with the possibility of skipping an undesired redimensioning step of the printed pieces for SEM analysis, Model 3 (Figure 4.2c) was designed with considerable smaller dimensions in order to be efficiently mounted on the SEM supports.

Finally, Model 4 and 5 (Figures 4.2d and 4.2e respectively) were developed having in mind the assessment of the piece's porosity content. Hence, having the same dimensions, these models only differ from each other in the mesh opening specification.

Respecting the whole process of producing 3D printed pieces, the most crucial stage is, undoubtedly, the preparation of the file that is going to be implemented by the printer. All the of the required steps to the production of a compatible file for printing, which will be described bellow, are preformed resorting to the printer's associated software, available for online download with no costs associated. Starting from the STL file obtained as described above, two main group of settings need to be defined using the printer's own processing software: support generation settings and slicing settings.

Supports are thin posts of printed material that lightly touch the printed model and are responsible for its adhesion to the platform in order to prevent the piece from floating in the vat. Some morphological aspects of the supports that will be generated such as the shape of the tip, the support's radius and lenght, the contact dept into the piece and the support angle must be determined by the user. As to radius and minimum length, the values chosen were the ones that provided a steady sustentation and, in addition, promoted a easy manipulation during post-processing. Regarding the contact dept and support angle, it was preferred to preserve the standard values provided by the software. Finally the *per se* support generation is achieved using the automatic tool provided by the software, having the user only to give one final input: the support density desired. For the unfolding of investigation inhere presented, this variable took the value of 75% of the piece's base area. This powerfull algorithm calculates the amount of supports required based on the piece's shape and orientation and places the needed supports in the correct orientation, defining the location of the support-model interface.

An illustration of the outcome described by the above indicated method is presented in Figure 4.3.

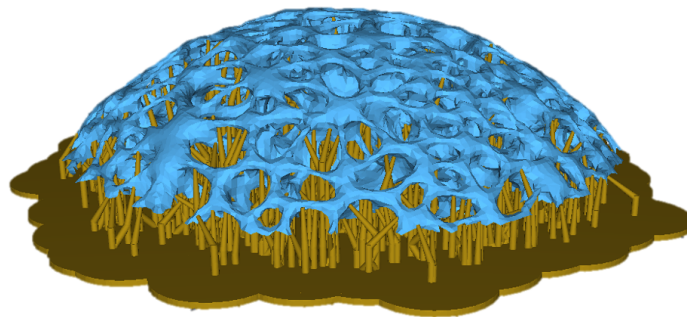


Figure 4.3: Outcome of the support generation process. In blue, the original piece provided to the software. In yellow, the support set generated for the sustentation the piece.

Following the support generation, the settling of the slicing details is necessary. The layer thickness determines the height of the suspension layer that is polymerized at once while the exposure time corresponds to the duration of the curing process of each individual layer. To note that a lower layer thickness correlates with an higher resolution and longer exposures will result in pieces with improved mechanical properties. However, these possible improvements are engaged with an inevitable increase of the total printing time which can be prolonged for many

hours. Thus it is vital to consider the trade-off between product quality and duration of the whole manufacturing process when defining the slicing settings. Off-time is the time interval between the curing of each consecutive layer; it corresponds to the time the platform takes repositioning itself for the next layer, allowing the fluid in vat to spread evenly on the printing area. Suspensions with higher viscosities require a lengthened off-time. Finally, the bottom layers, compact layers from which the supports arise, are responsible for the attachment of the piece to the platform and, as result, must be polymerized during superior time periods when comparing to the ones of the following layers, promoting higher stability.

The slicing specifications used were defined after an optimization process resulting of several months of intense 3D printing trials.

The software creates a file with a format compatible with the printer that consists on a set of images that will be sequentially displayed by the printer's LCD screen in order to cure each layer. Hence, each image corresponds to distinct cross sections of the piece as result of the defined layer thickness based slicing (Image 4.4).



Figure 4.4: Different cross sections of a model for 3D printing as seen in the printable file. Cross section relative to the bottom layers (left), cross section relative to the initial generated supports (center), cross section relative of one model layer (right).

This file can be easily uploaded to the printer using a regular USB stick and, after pouring the selected suspension (Section 3.3), the 3D printing process begins.

The printer provides real-time information regarding the on going printing job, namely, percentage of work depleted, expected remaining printing time and number of layers that still need to be polymerized to produce the final piece. These displayed technical details may be crucial to the success of the job and allow the user to take fundamental precautions such as refilling the vat with the printing suspension, which is necessary due to the limited amount of suspension that can be poured at one time. Longer prints with bulkier pieces that require more material can be paused at any time in order to supply more suspension.

4.1 Post-printing procedure

After printing and removing the platform from the equipment, with the help of a smooth edged spatula, the produced pieces are detached from the platform with care. The piece is submitted

to a deep chemical washing procedure in isopropyl alcohol in order to remove the excess non-polymerized superficial portion of the resin-based suspension that may still be deposited around the piece and supports are then removed resorting to a small plier.

Following the rinsing, a post-curing treatment is applied, exposing the recently printed piece to an UV lamp with an approximated wavelength of 400 nm to enhance the mechanical properties, promoting strength and stability of the printed piece.

The final step consists in the application of a sintering cycle to the 3D printed sample with two major and very distinct purposes: removing the photosensitive resin and enhancing the mechanical properties of the piece. Therefore, in order to guarantee the fulfillment of both goals successfully, a two-step sintering was the approach chosen for the thermal treatment, inhere graphically presented in Figure 4.5.

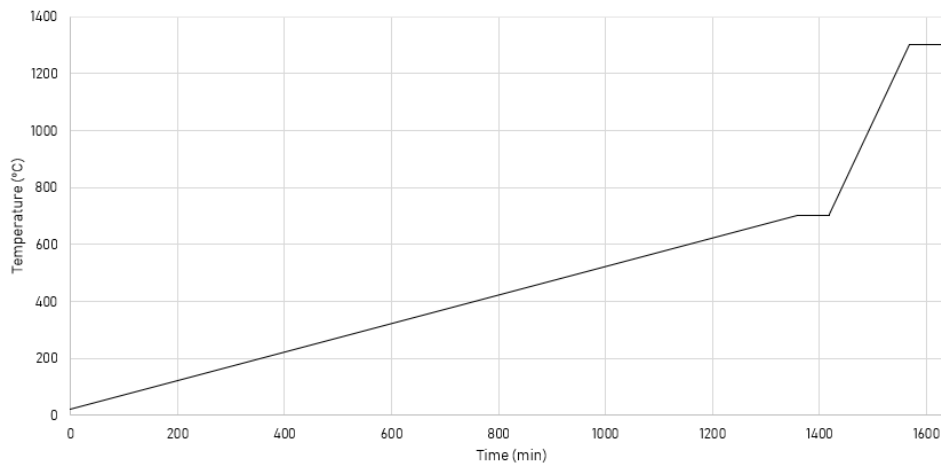


Figure 4.5: Heating curve for firing treatment of 3D printed pieces.

The first step of the sintering process consists in a slow heating ramp of a 0.5 °C/min rate up to 700 °C, temperature that is then kept unchanged during one hour. These specific parameters promote the maximum resin burn-out required to the production of biocompatible scaffolds for implantation, without affecting the piece's integrity and were defined by the resin provider's indications.

In the second step, the sample is fired up to 1300 °C with a heating rate of 4 °C/min and held at the final temperature for one hour. This phase is the responsible for the formation of one final solid piece, stimulating the consolidation of the ceramic particles, allowing the sintering process to occur.

Ultimately, the piece is let to cool until it reaches room temperature.

These above mentioned post-processing steps, are highlighted in Figure 4.6 as a visual reference that illustrates the piece's progression until it reaches its final form.

As an alternative approach to the above mentioned post-processing procedure, some of the printed pieces were subjected to a P_2O_5 -CaO based glass immersion in a attempt to reinforce the sample's mechanical properties.

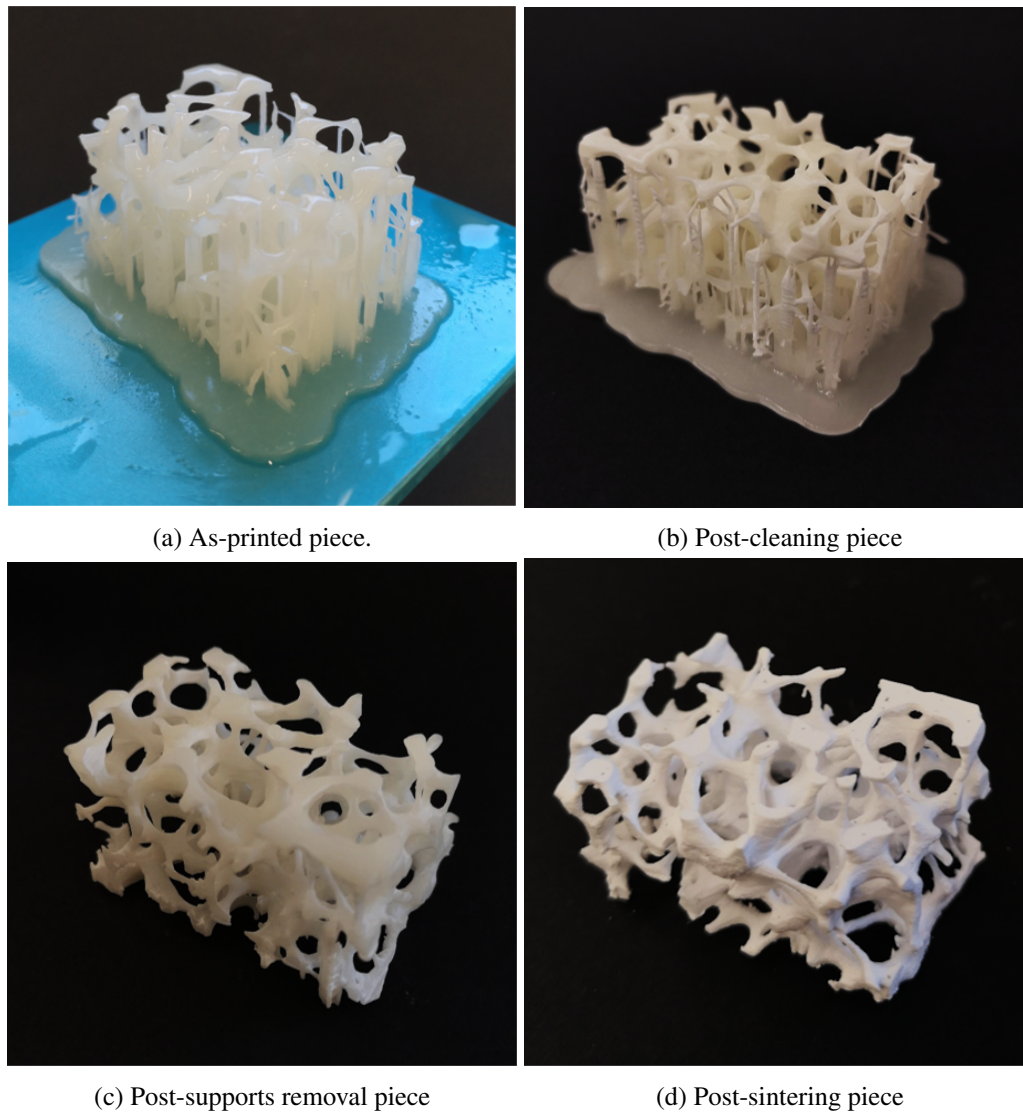


Figure 4.6: Visual representation of the post-printing procedure applied to a piece.

Therefore, after printing, the supports are removed, the piece is cleaned likewise the standard post-processing treatment and, after being UV cured, it endures a pre-sintering firing treatment. First the temperature is raised at $0.5\text{ }^{\circ}\text{C}/\text{min}$ up to $700\text{ }^{\circ}\text{C}$ and is then kept at this plateau for one hour to meet the same propose as described aboved. However, the following conditions, respecting heating rate and dwell time, depended upon the sample's geometrical shape. The piece is let to cool inside the furnace and is then immersed in a boiling glass solution. Finally, it endures a final heating treatment up to $1300\text{ }^{\circ}\text{C}$ in order to promote the ceramic's sintering.

Chapter 5

Results and discussion

5.1 Resin

Due to the lack of information concerning the chemical identity of the resin and in order to confirm the few data disclosed, a Fourier-transform infrared spectroscopy analysis was performed. The obtained vibrational spectrum, presented in Figure 5.1, can be labeled as the organic fingerprint of the analyzed sample and it is the result of the electronic radiation absorption for specific frequencies which is linked to the vibration of each particular group of chemical bonds within a molecule.

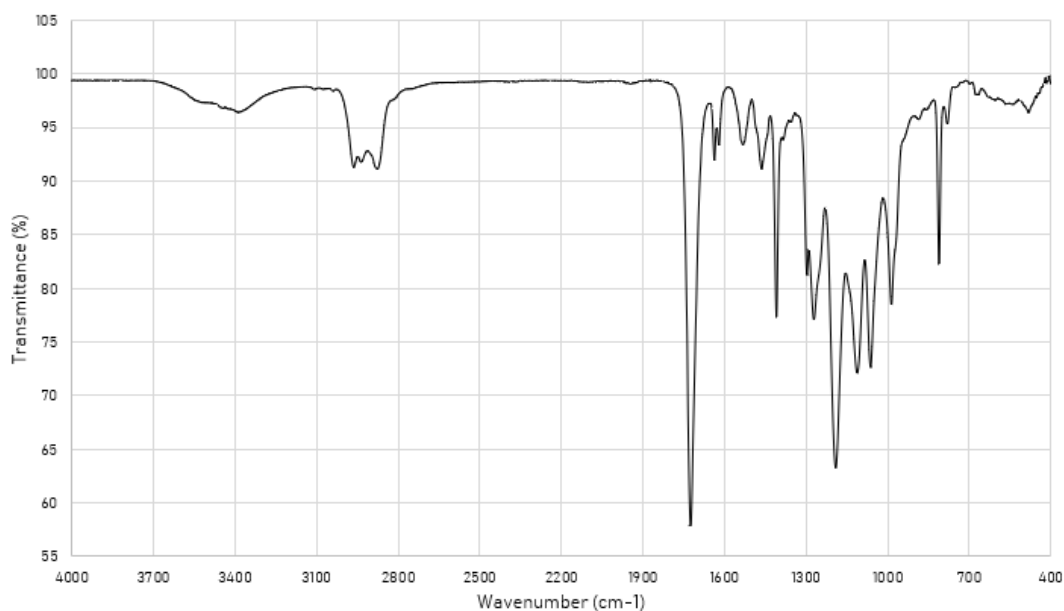


Figure 5.1: Fourier-transform infrared spectroscopy spectrum of the resin.

The identified acquired peaks correspond to the ones of a poly(methyl methacrylate) FTIR spectrum, allowing the deduction that the resin is, indeed, a methacrylated based resin [59, 60].

The peak assignment of the sample's vibrational modes can be found in Table 5.1.

Table 5.1: FTIR peak assignment for the resin sample.

Wavenumber (cm ⁻¹)	Peak assignment
3000-2800	Stretching vibration of -CH ₃ and -CH ₂ groups
1723	Stretching vibration of C=O
1635	Stretching vibration of C=C
1490-1275	Different CH ₃ and CH ₂ vibrational modes
1269	Symmetric stretching vibration of C-C-O
1189	Skeletal chain vibration
1061	Stretching vibration of C-O
984	Bending vibration of O-CH ₃
900-750	Different CH ₃ and CH ₂ vibrational modes

One must consider the resin only as a printing vehicle that needs to be eliminated to achieve the final piece composition since this work's objective is the production of a scaffold as close to purely ceramic as possible and, also, due to the fact that the resin was not formulated having in mind possible biomedical applications.

When considering the resin's removal, it comes intuitively the hypothesis of resorting to the thermal treatment not only to enhance the mechanical properties of the 3D printed models but also to promote the resin burn-out.

To note that only the organic portion will burn-out and the prevailing ashes from the application of high temperatures in the presence of an oxidizing agent correspond to the inorganic remains after the elimination of the water and organic compounds from the sample.

A first approach to determine an approximate relative amount between the organic and inorganic phases was carried out since a predominantly irremovable inorganic composition of the resin would immediately put in jeopardy its use in the production of the desired scaffolds for bone regeneration.

For that, three large pieces of previously polymerized resin were separately weight in before and after being submitted to the same heating cycle used for the 3D pieces production in order determine the amount of mass lost, easily linked to the organic-inorganic composition distribution within the sample. The obtained results reveal mass loss values in the 99% order (See Table 5.2).

It is clear that, even tough this preliminary analysis may not deliver entirely accurate and trustworthy results due to its modest nature, the great majority of the chosen resin's components are eliminated during the appliance of the heating cycle.

Thereby, one can quickly conclude that the resin's composition is mainly organic and be easily eliminated from a printed piece during the sintering cycle, remaining only a vestigial portion of inorganic residues.

The above-mentioned findings disclose this resin as a very promising foundation material to the production of 3D printed bone scaffolds. However, in order to cross-check the results and

Table 5.2: Obtained results for the organic-inorganic relative composition analysis of the resin using two different approaches.

	Furnace burn-out approach	Thermogravimetric analysis
Lost mass (%)	99.8	93.01

obtain values that may approach more truthfully to the actual organic-inorganic relative phase composition of the resin, an additional test, more rigorous was carried out: a thermogravimetric analysis.

The thermogravimetric analysis is a destructive thermal analysis that simulates, in a controlled environment and delivering information as close to reality as possible, the procedure described above. It allows a continuous monitoring of the sample's mass oscillations over time with increasing temperature. The acquired data is displayed in Figure 5.2.

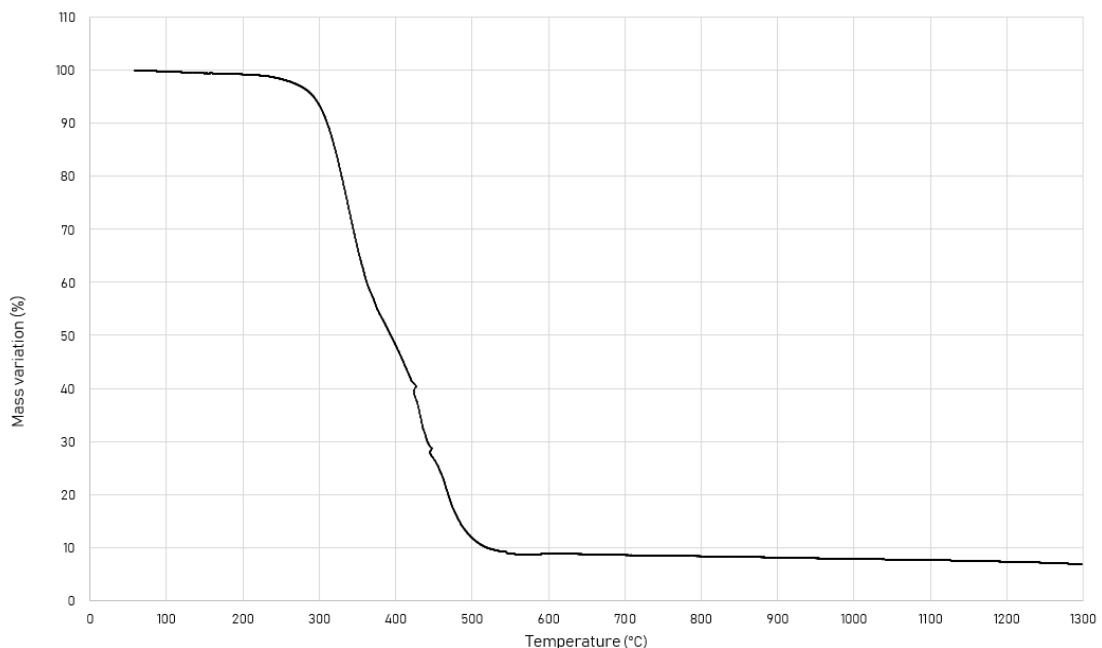


Figure 5.2: Resin's thermogravimetric analysis curve.

The first evidence to extract from these results is that it is in the 300 °C to 500 °C heating interval that the most accentuated mass loss is recorded, with the burn-out of approximately 80% of the sample's total mass. However the final mass loss value, 93.01%, does not correspond to the one registered while resorting to the previous approach, which registered a nearly to total burn-out. This slight discrepancy was already predicted since the original approach is very prone to the promotion of material loss during the manipulation of the heated sample's remains either during the withdrawal from the furnace or weighing.

Even though it has already been proved that the resin's largest fraction is removed from the

sample during sintering, it is of vital importance to scrutiny the remaining portion that will be accommodated within the implantable 3D printed piece that, regardless of being a very limited amount, may be enough to foment an extreme adverse biological response and thus, reducing its viability as a solution.

The energy-dispersive X-ray spectroscopy applied to the resin's ashes and which results are presented in Figure 5.3, reveal silicon as the main constituent of the fraction of the resin that will remain in the final pieces, followed by oxygen.

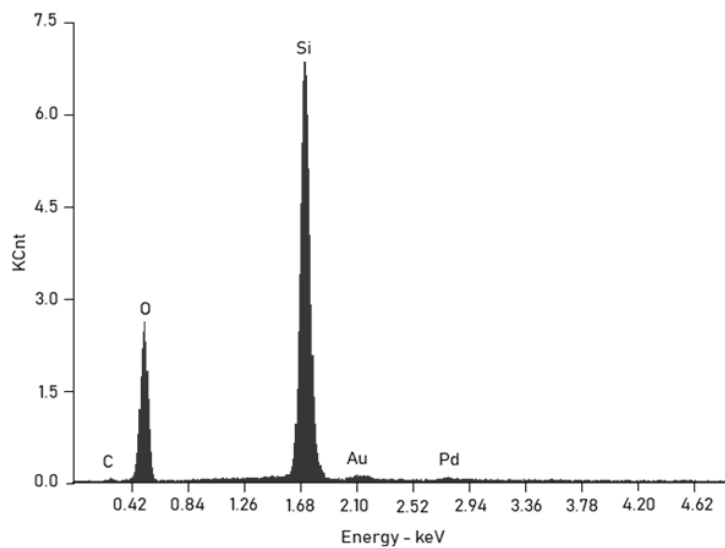


Figure 5.3: Energy dispersive X-ray spectroscopy results for the resin analysis.

It was not expected or even considered that the resin remains themselves could possibly influence positively the bone formation process but, in fact, the role of silicon as a bio active signal for bone tissue engineering was first reported by Edith Carlisle in 1976 and has been attracting a lot of attention for the last years [61]. Even though few studies to clarify the biological functional effects of each individual component of a complex bioceramic material have been presented due to the clear preference of the overall material's properties analysis, some published works have already reported the valuable role of Silicon and Silica in bone formation as result of their ability to promote osteostimulation and osteoconduction, supporting cell adhesion, proliferation and differentiation while activating angiogenesis [62, 63]. In fact, an appropriate concentration of silicon ions can be considered mitogenic for bone cells, boosting the osteoblast proliferation, and their release can be linked to antibacterial properties due to the pH increase in the surrounding environment [63, 64]. Furthermore, *in vivo* studies have defined the cytotoxic effects of silica-based porous materials as null or extremely low for diverse cell lines and many authors have already started adding silicon to a relatively broad range of calcium phosphate based materials as a doping agent [65, 66]. Taking this facts in account, one can assume that the Silicon presence in the inorganic remains of the resin will, at least, not play a negative role towards the final objective.

The presence of the residual gold and palladium peaks is a predictable consequence of the thin film that was sputtered on the sample to enhance electron conductivity.

5.2 Hydroxyapatite powders

Particle size and shape are some of the primary features that can be used to characterize a powder. Furthermore, along side with others, these features highly influence the powders' properties, particularly the future suspension's rheological characteristics, and, consequently, their potential applications. Thus, the opening study of the different hydroxyapatite powders consisted in a granulometric analysis to identify the particles' size distribution and in a morphological assessment resorting to scanning electron microscopy. Figure 5.4 and Figure 5.5 present the obtained results.

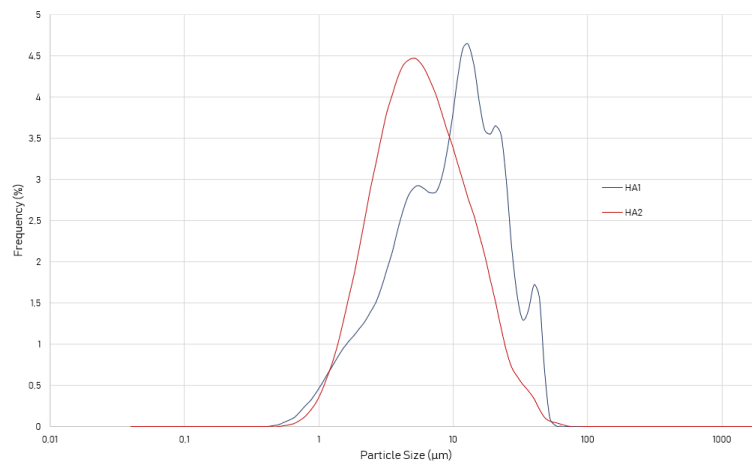


Figure 5.4: Granulometric analysis of the HA powders.

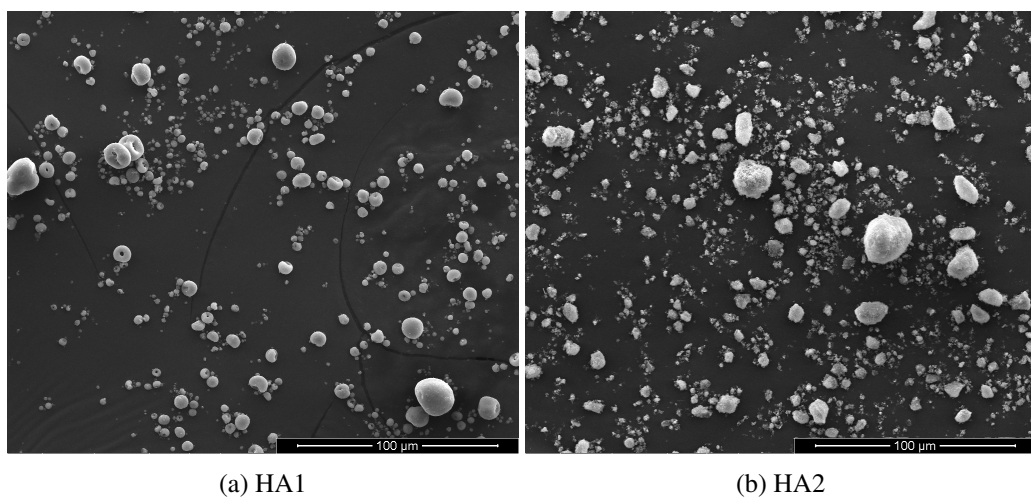
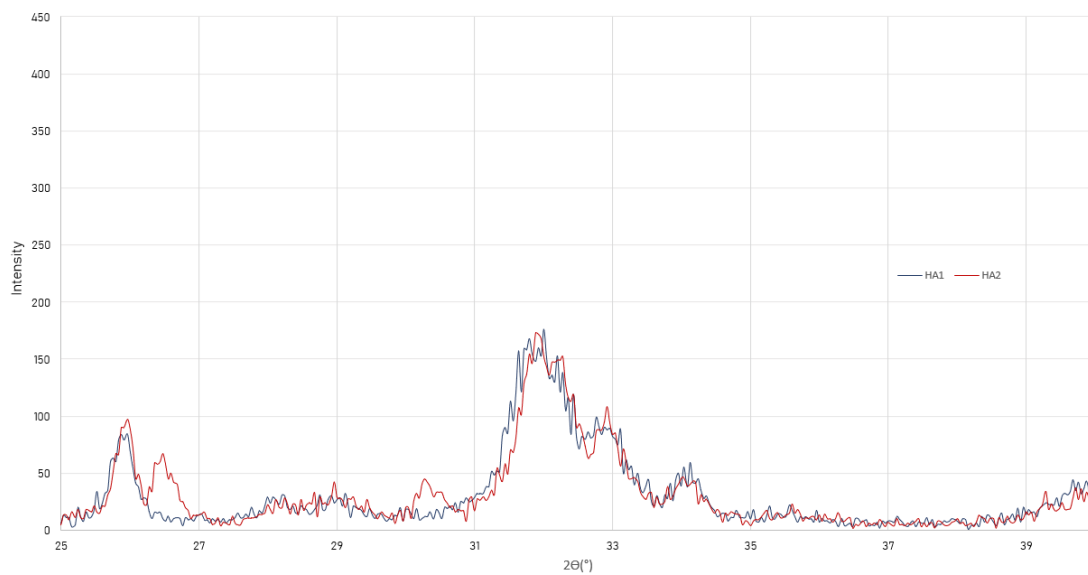


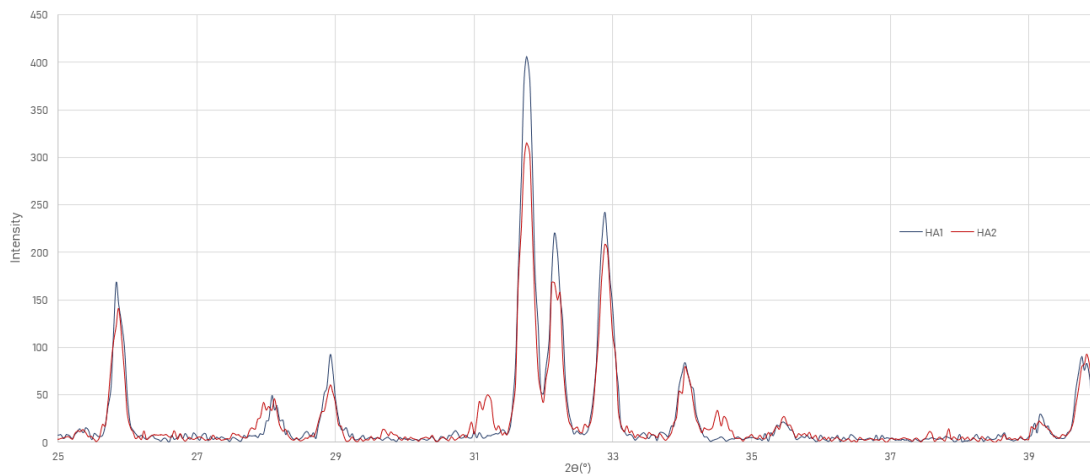
Figure 5.5: Scanning electron microscopy images for morphology assessment of different HA powders. 1000x magnification, secondary electron mode.

The particles that comprise the HA1 powder present a very consistent spherical shape (Figure 5.5a). However, when analyzing the granulometric results, it presents a relatively irregular dispersion with a D50 of $10.66 \mu\text{m}$ and standard deviation of 10.79.

In turn, the particles of the HA2 powder, despite not being so regular in size as the ones of HA1, present a close to spherical form (Figure 5.5b). As to the granulometric analysis, the D50 of the sample is lower than the previous one with a value of $5.88 \mu\text{m}$ but the dispersion matches more closely to a normal distribution with a standard deviation of 7.47.



(a) Pre-sintering powders



(b) Post-sintering powders

Figure 5.6: Combined diffractogram of the two HA powders analysed through XRD.

Following this preliminary powder analysis, further testing was carried out. To study each powder's detailed structure, namely the specific phase composition so that their quality can be

assessed to validate their use for the current and future investigations, a X-ray diffraction analysis was carried out, before and after sintering the powders. The experimentally obtained resulting spectra are presented in Figure 5.6.

This characterization technique can only identify crystalline phases so, from the results that reveal non-distinguishable peaks presented in Figure 5.6a and as anticipated, one can conclude that the analyzed powder corresponds to a low crystallinity material, probably due to its production method, presumably by precipitation processes.

The position and intensity of the registered peaks from the post-sintering analysis were cross-checked against referenced values [67] of relevant expected phases (See Table 5.3) in order to determine the semi-quantitative crystallographic phase composition of the different powders.

Table 5.3: Inorganic Crystal Structure Database Referenced (ICSD) informations for the analysis of the obtained diffractograms. Adapted from [67].

Crystallographic phase	Chemical formula	ICSD code	2θ value for maximum intensity
Hydroxyapatite	$\text{Ca}_{10}(\text{PO}_4)_6(\text{OH})_2$	01-076-0694	31.771
α -tricalcium phosphate	$\text{Ca}_3(\text{PO}_4)_2$	00-029-0359	30.710
β -tricalcium phosphate	$\text{Ca}_3(\text{PO}_4)_2$	01-072-7587	31.013

Coupling the values from Table 5.3 with the data obtained from the diffractograms (Figure 5.6b), one can easily extract the crystallographic phase relative composition for each sample which can be found in Table 5.4.

Table 5.4: Identification of crystallographic phases and their relative contribution for the composition of each HA powder.

		HA powder			
		HA1		HA2	
		Peak Intensity	Relative composition (%)	Peak Intensity	Relative composition (%)
Crystallographic phase	HA	406	>98	315	88
	α -TCP	5	-	6	-
	β -TCP	5	-	43	12

From these results, it is noticeable that the phase composition of the HA1 powder after the heating treatment closely match to a nearly pure phase hydroxyapatite as result of the correct stoichiometric Ca/P ratio use upon production.

On the other hand, the HA2 powder, in addition to the hydroxyapatite crystallographic phase with a relative value of 88%, is also composed by a considerable β -TCP phase, 12%, that was not identified in the HA1 sample.

Even though a pure phase HA powder may come into sight as very appealing result it is important to note that a biphasic calcium phosphate can also be very interesting as synthetic bone

graft. When implanted, hydroxyapatite presents a relatively slow biodegradation, whereas a β -TCP scaffold will be absorbed and substituted by bone more easily, promoting a profound bone remodeling in the surrounding areas [68, 69, 70].

With this in mind, HA/ β -TCP biphasic calcium phosphates, such as the HA2 powder, reveal themselves as an also promising material for bone grafting due to its mixed nature that is responsible for an in-between degradation rate when implanted [71]. For these aforementioned biphasic calcium phosphates, an higher HA/ β -TCP ratio is bounded to a lower dissolution rate of the synthetic bone scaffold [71].

As to chemical evaluation, a zeta potential measurement was performed and the obtained results are presented on Table 5.5.

Table 5.5: Zeta otential value for the different HA powders.

	HA powder	
	HA1	HA2
Zeta potential (mV)	-20.6	-15.6
Standard deviation	0.794	0.208

The obtained values are negative, as expected for calcium phosphate materials, and it is believed that this characteristic may be profitable for the bone regeneration process, promoting cell activity [72]. The observed value divergence between the two powders reflect the their chemical differences.

5.3 Formulations

One of the most important characteristics that should be analyzed when studying the behaviour of suspensions is their viscosity. For that, viscosity determinations tests were performed and the obtained results as well as the ones respecting the resin are displayed in Figure 5.7.

First, considering an intra-powder analysis, it was observed that the viscosity values increased as function of the solid content, and in this way, the lowest solid load used (L1) is associated to the production of the less viscous formulation within each individual powder. Ideally, the printable suspensions should be prepared with the highest amount of HA powder possible, preferably with a 40 wt% or higher content of particles to assure an high densification of the printed body [53]. However, when working with large concentration levels of powders, the particles tend to pack together and the amount accessible resin to promote the relative particles' motion starts to decrease, having as a direct consequence a rapid increase of the suspension's viscosity [73]. In this way it is important to balance these two incompatible goals and optimize the formulation as possible, having always in mind the associated trade-off.

Concerning the observed differences in the rheological properties that rise into sight when analyzing the results of the suspensions prepared with different base powders, the particle size

and particle size distribution must be considered. It has already been reported that lower particle diameters are linked with higher viscosity values and that broader particle size distributions promote a reduction in the suspension's viscosity [74]. In this way, it is rational for the HA1 powder formulations to display significantly inferior viscosity values as its particle size and particle size distribution are higher than the one's of the HA2 powder.

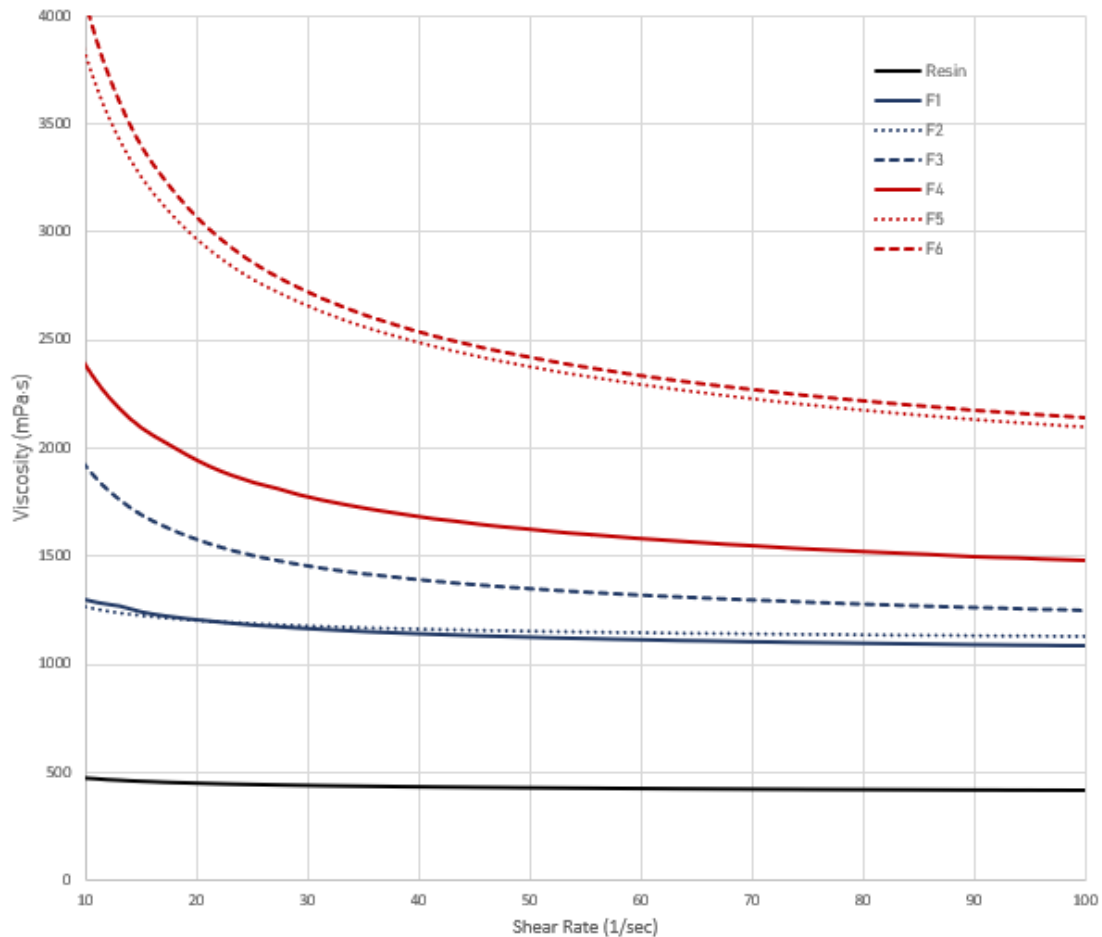


Figure 5.7: Treated data concerning the viscosity determination of the different formulations. In blue, HA1 powders formulations' curves. In red, HA2 powders formulations' curves.

Even though, the main viscosity's variations within the different formulations have already been interpreted, it is still necessary to guarantee their 3D printability. The rheological properties of a printable suspension highly impact the success of a piece's production. When 3D printing, high viscosity levels hinder a correct flow of the uncured suspension from small already polymerized channels that may, ultimately, put in jeopardy the obtention of pieces with the desired design. Griffith *et al.*, while developing a photocurable resin for AM techniques, defined a viscosity range that assure the suspension's printability, simplifying in this way formulation's selection process. The upper limit after solid load incorporation of this crucial feature was set as 3000 mPa.s [53]. Concerning the acquired data, for higher shear rates, when the viscosity values tend to reach a steady plateau, all of the designed formulations are well under the defined limit, hence can be

considered as suitable candidates for the 3D printing process.

5.4 3D printed pieces

Even though formulation F4, F5 and F6 were within the viscosity range defined in the previous section, when printing with them, only using smaller, and consequently quicker, files, successful results are achieved like the one presented in Figure 5.8. It is believed that the sample's slight blue colour that comes into sight after the sintering process is induced by the trace of the manganese element in the powder [75].



Figure 5.8: Post-sintering 3D printed piece (HA2).

The difficulty linked to these formulation's printing can probably be explained by analyzing the rheological properties' alteration with time, since the HA2 formulations start to thicken up and acquiring a soggy appearance, making the 3D print, with time, increasingly difficult or even inconceivable.

Even though no evidences were collected, it is possible that the β -TCP phase is more soluble in the resin than the HA one. As follows, the HA2 powder, having an higher relative amount of the β -TCP phase, will register an higher powder dissolution.

On the other hand, the particle size of the HA2 powder is comparatively smaller than the ones that compose the HA1 powder, hence, leading, to an higher surface area that will lead to a increased dissolution rate [76].

In this way, even though the use of the HA2 powder may be of great interest in the production of these scaffold's, as reported in Section 5.2, was for now discarded in order to achieve a more methodical and exhaustive investigation of the overall process without printing instability.

The printable parameters defined were selected in order to guarantee the successful pieces' print using the stable HA1 formulations. Some of these particular printed pieces are presented in Figure 5.9.

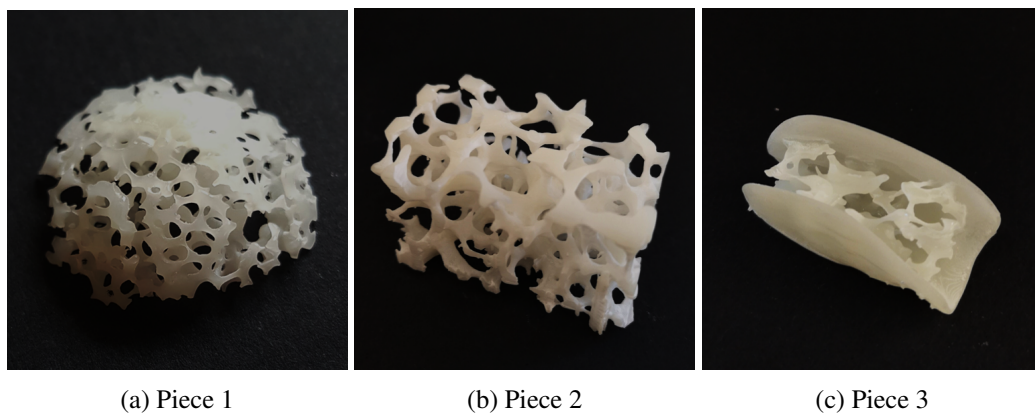


Figure 5.9: Pre-sintering 3D pieces (HA1).

A pure phase hydroxyapatite with the 1.67 stoichiometric Ca/P ratio as the HA1 hydroxyapatite remains thermally stable without suffering any phase transformations when heated as far as 1400 °C [77].

However, some external variables may affect the powder's thermal stability during the required heating treatment applied to the piece so, it is necessary to understand the possible phase transitions that may occur. Starting with the XRD acquired data, graphically presented in Figure 5.10, and following the same method as the one described above, it was possible to estimate each crystallographic phase relative composition. The attained values are displayed in Table 5.6.

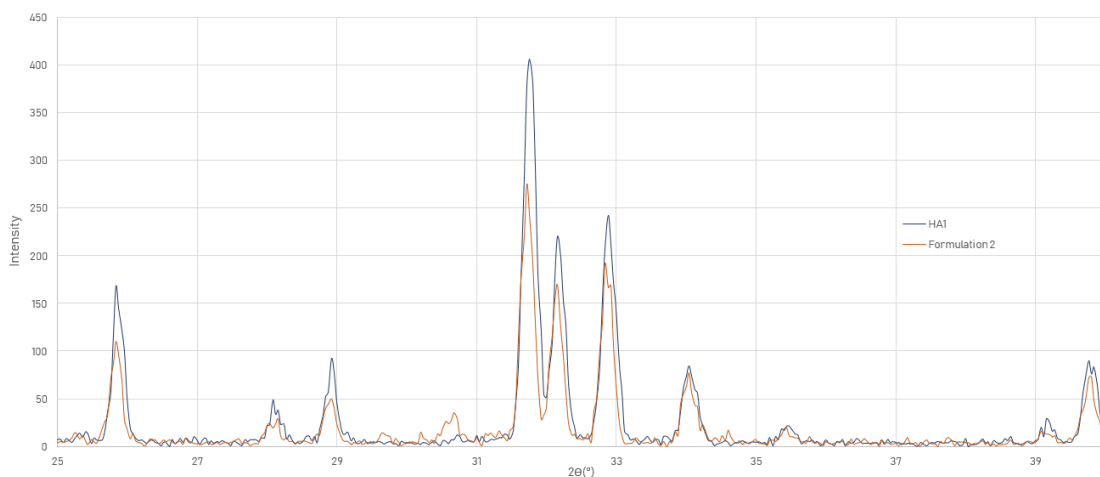


Figure 5.10: Combined diffractogram of a printed formulation (Formulation 2) and the respective calcined powder (HA1) analyzed through XRD.

From the results presented, it is possible to infer that the 3D printing and the post-processing procedure actually induce crystallographic phase transformations as perceptible when comparing these results to the one's presented in Table 5.4.

However, even though the temperature didn't surpass the 1400 °C plateau, the recorded phase transformation promoted an unexpected appearance of the α -TCP crystallographic phase. This

Table 5.6: Identification of cristallographic phases and their relative contribution for the composition of the printed piece (Formulation 2).

		Peak intensity	Relative composition (%)
Crystallographic phase	HA	275	90
	α -TCP	29	10
	β -TCP	4	-

can probably be explained by the silicon residues from the resin's inorganic remains that persist in the final piece; a silicon substitution within the HA structure destabilizes it and, when the powder is heated up to over 1100 °C, favors the thermal transformation of HA into α -TCP [78].

Being the scaffold's tailoring according to the patient's specific needs the prime objective of a future market implementation of this product, it is of extreme importance to match the piece's dimensions to each individual defect.

In this way, it is fundamental to quantify the piece's shrinkage associated to the ceramic firing treatment in order to estimate the required scaling of the original design to, ultimately, achieve the correct proportions. The results of this assessment are presented in Table 5.7.

Table 5.7: Contraction values of 3D printed pieces after firing.

Formulation	Heating treatment applied	Contraction (%)			
		x	y	z	Volumetric
F1	Sintering	28	28	29	63
F2	Sintering	36	37	37	74
F3	Sintering	38	39	38	76
F2	Pre-sintering	17	17	20	44

When comparing the contraction values of two samples which were prepared from the same foundation formulation but submitted to different heating cycles, one can perceive that the applied temperature does have a major impact in the piece's global shrinkage coefficient; the piece that only endured a pre-sintering, presented a contraction value of 44% while the one that withstood a full 1300 °C sintering contracted in the 70% order. Taking into consideration that the ceramic body only starts to contract at 1000 °C, peaking at 1250 °C, it is not abnormal for the pre-sintering piece to present a very reduced comparative shrinkage value since this temperature range was not achieved and maximum densification was not consummated [77]. Concerning the powder incorporation variation, it is noticeable that as the amount of HA powder incorporated in the suspension rises, the associated sample's contraction is bigger, when using the same firing settings. In fact, this result was already forecasted as the solid loading of the ceramic slurry highly influences the piece's contraction since lower solid loads are connected to an higher pore content that, in turn, is responsible for lower amounts of contraction [79]. It is natural, in this way, that Formulation

1 gives rise the lowest contraction value (63%), while, with an approximate shrinkage of 76%, pieces printed with Formulation 3 are the ones that contract the most. Having this analysis been finished, and taking into consideration the fact that the contraction values within the different axes do not present significant differences, it is conceivable to speculate that a unique shrinkage coefficient applied to all of the design's dimensions during the modeling step can have as an outcome high quality pieces. However it is important to emphasize that this value is specific for each solid load and, consequently, has to be defined in advance.

For the calculation of the scaffold's total pore content, it was necessary to deduce the actual real piece's volume and, for that, each phase contribution towards the overall volume was evaluated resorting to previously uncovered relative phase composition of a printed piece and to each phase's specific density value, discriminated in Table 5.8.

Table 5.8: Reported theoretical density values for the different crystallographic phases. From [80].

Crystallographic phase	Theoretical density (g/cm ³)
Hydroxyapatite	3.156
α -tricalcium phosphate	2.863

This method was applied to different pieces 3D printed from two different models that differed on the structure's mesh opening: Model 4, with a more open mesh and wider pores, and Model 5 that presents a intricate network, resulting on a smaller mesh opening (See Figure 5.11). The obtained results can be discerned in Table 5.9.

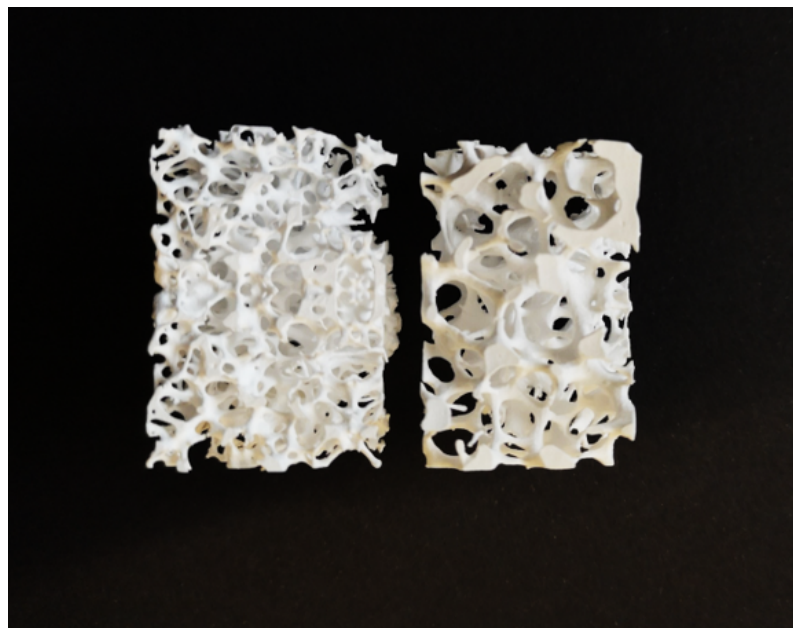


Figure 5.11: Post-sintering 3D pieces for porosity assessment (Formulation F2). On the right, piece produced from the Model 4 file. On the left, piece produced from the Model 5 file.

A simple preliminary comparative assessment of the disparity between the density values of the crystallographic phases and the one correspondent to the overall piece density, extrapolated from the sample's weighing and measurement, allow a clear realization that, indeed, the pore content is profoundly significant to the scaffold's structure.

Table 5.9: Porosity evaluation results.

Formulation	Model	Apparent volume of the piece (cm ³)	Apparent density of the piece (g/cm ³)	Real volume of the piece (cm ³)	Pore content (%)
F3	4	9.02	0.23	0.66	93
	5	10.07	0.25	0.80	92

When quantitatively analyzing the results, one can conclude that both piece's pore content nearly match. This result came with no surprise because both the models were created having as starting point the same original trabecular structure for the model design, and it is even possible to conjecture that the 1% divergence is probably due to minor operation errors that took place during measurements. In this way, since all the dimensions were kept proportional during the model manipulation it was also expected for the pore content to match. It is important, however, to emphasize that 3D printed pieces with a more closed mesh design are easier to manipulate as the more dense structures avoid the scaffold's fracture upon contact.

These findings stand as excellent indicators for the future use of the scaffold's, namely this particular design, as it is possible to manipulate the mesh to match the desired pore size while maintaining an above 90% pore content ideal from bone regeneration [81].

Obviously, it would be interesting to match the printed scaffold's mechanical properties to the ones of the natural trabecular bone and even tough resistance to compression force was not possible to determine due to the lack of an appropriate load cell, it quickly became evident that the initial printed pieces exhibited a very low resistance to compression, easily crumbling upon contact.

As a consequence, rose the possibility to adapt the idea of glass reinforced hydroxyapatite composites in order to boost the piece's mechanical properties [82]. A phosphate based bioglass was incorporated via immersion, aiming to serve as sintering aid and promoting a liquid phase sintering route. During sintering, the glass particles fuse and the liquid spreading improves the diffusion mechanism by acting in the HA particles, reducing the interfacial energy and minimizing the porosity [83].

To verify the glass incorporation within the printed piece, two different samples produced with the HA1 powder and with a L2 load (Formulation 2) were analyzed trough SEM: one regular and one submitted to the bioglass incorporation procedure. The obtained images are presented in Figure 5.12.

The visual disparity between the two samples is evident. While in Figure 5.12a it is possible to recognize individual powder particles with clear distinguishable borders, in Figure 5.12b,

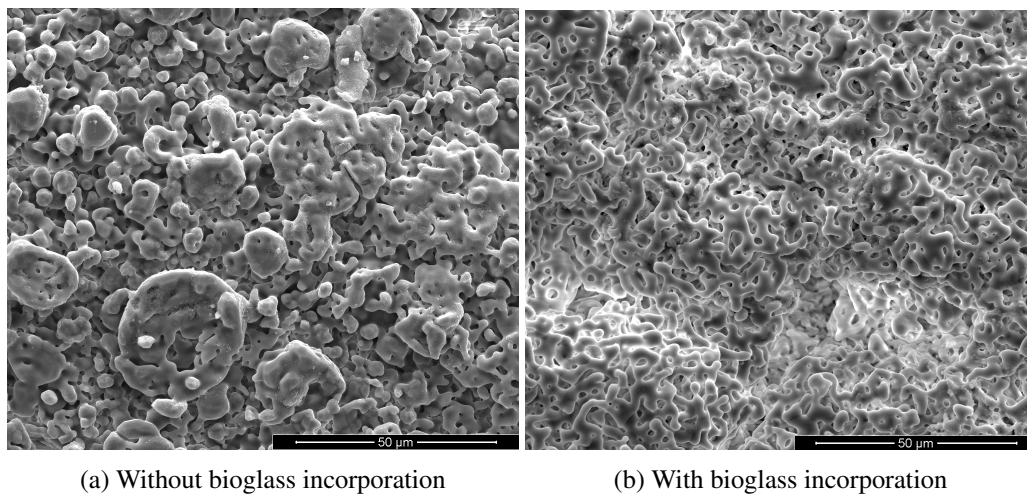


Figure 5.12: Scanning electron microscopy images for bioglass incorporation assessment in 3D printed pieces (Formulation 2). 2000x magnification, secondary electron mode.

relative to the bioglass immersed piece, the same particles seem fused together to a higher extent, creating what appears to be a more homogeneous and dense structure. These results may suggest that, indeed, the bioglass positively influences the optimization of the sintering process, thus conferring superior mechanical properties to the printed piece. Further, these findings are in concordance with the non-quantitative assessment made when simply manipulating the models; the bioglass immersed pieces, undoubtedly, endure the application of forces more intense than the ones possible to apply to classically produced pieces with a regular post-processing procedure.

Still concerning the bioglass incorporation, additional investigation was performed, namely a X-ray diffraction analysis, as it was possible for the bioglass to stimulate the formation of secondary crystallographic phases during the temperature rise. The acquire and treated information is presented in Figure 5.13 and Table 5.10, respectively.

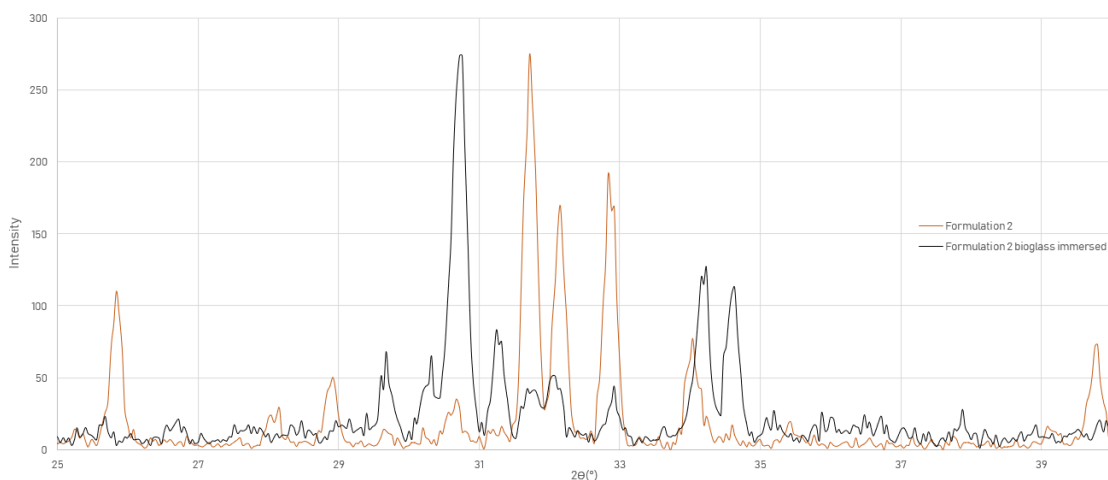


Figure 5.13: Combined diffractogram of a printed formulation (Formulation 2) and the respective bioglass immersed piece analyzed through XRD.

Table 5.10: Identification of cristallographic phases and their relative contribution for the composition of the bioglass immersed printed piece (Formulation 2).

		Peak intensity	Relative composition (%)
Crystallographic phase	HA	39	12
	α -TCP	274	84
	β -TCP	12	4

The disclosed findings exposed a very surprising result: a big crystallographic phase transition from HA into TCP took place.

This unexpected development required a substantial explanation and, as a result, to infer if the cause of such transformation was promoted by the double heat treatment used and not the immersion itself, a sample without bioglass incorporation, but submitted to the double heat treatment, was analyzed by XRD. The obtained diffractogram is presented in Figure 5.14.

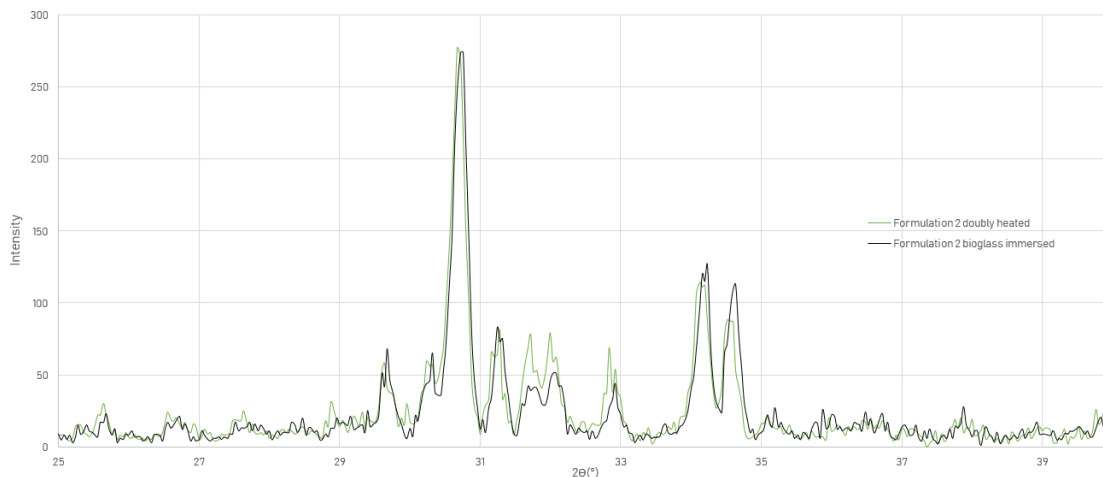


Figure 5.14: Combined diffractogram of a bioglass immersed piece (Formulation 2) and the respective piece for sintering control analyzed trough XRD.

Again, an identification of cristallographic phases and their relative contribution for the overall composition of the piece took place. The results are displayed in Table 5.11.

Table 5.11: Identification of cristallographic phases and their relative contribution for the composition of the printed piece for sintering control (Formulation 2).

		Peak intensity	Relative composition (%)
Crystallographic phase	HA	78	21
	α -TCP	277	73
	β -TCP	22	6

From the results it is clear that the double heat treatment is the most important factor for the extensive transformation of HA into TCP phases and that this must be a result of a synergetic

effect of Si and the severe heating cycle.

However, even though not being the main responsible for the phase transformations, the bioglass immersion does promote further HA conversion into TCP due to above mentioned synergetic effects combined with the bioglass treatment.

These findings consist on a major concern towards the future applications of the described immersion method as a scaffold with a large content of the α -TCP will have an extremely high rate of *in vivo* resorption [84].

Chapter 6

Conclusions and Future Work

A new method, using DLP technique, for the production of bone scaffolds was proposed and validated attaining high quality tailorable 3D pieces that mimick the complex bone structure.

The preparation of the file for 3D printing is one of the most crucial and sensible steps when applying this technique. Several settings can be manipulated when preparing the file, however, the ones that mostly impact the print's success and quality were the layer thickness and the exposure time. Smaller layer thicknesses can produce structures with higher resolution levels while high polymerization times are decisive to a good piece's fixation, promoting its stability during the printing process. On the other hand, it is important to note that with the reduction of the layers' thickness and the increase of exposure time, the expected printing time will exponentially increase which may be a problem when using unstable suspensions.

Regarding the prepared formulations, the powder with which the best results were achieved is the HA1 due to the higher particle size and the larger size distribution range. These characteristics are responsible for the production of suspensions with high load levels and low viscosity values which is extremely important for the final 3D printing outcome. Incorporation of substantial powders loads to improve the structure's mechanical properties may sound appealing, however the formulation's viscosity limit has to be respected according to several authors.

The approach involving a post-treatment by a glass immersion was proven not only to improve the piece's mechanical resistance but also to promote extreme thermal transformations into TCP phases during sintering. In this way, the decision to follow this strategy or not must be carefully considered, as there is an inherent trade-off between the piece's resistance and dissolution rate upon implantation.

Even though it still has large improvement potential that can be explored, it is clear that the developed process in this dissertation consists in an innovative and useful tool towards the improvement of the current bone graft field.

Despite the promising results achieved, further work needs to be done in order to optimize the preparation process and the performance of the final 3D printed products.

Firstly, concerning the printable ceramic suspensions, increments on the solid load content should be optimized as the viscosity limit for their use in the DLP printing was not yet achieved, ie

3000 mPa.s. Higher amounts of powder incorporated in the formulation will produce 3D structures with higher compression resistance that ultimately could avoid the necessity of applying the extra bioglass immersion post-processing step. At the same time, and in order to achieve the objective above mentioned, there is a need to control the particle size distribution and particle size and shape of the raw powder HA. Powders from different providers should be explored in order to guarantee the best powder characteristics to ensure the stability of the ceramic suspension and, therefore, consistently successfully printed structures.

In addition, it would also be interesting to create an original resin formulation that would allow the transformation of this production method into an self-sufficient one, reducing resin costs and, therefore, decreasing the overall cost production for future commercialization of these products.

Finally, it is of utmost importance to determine the mechanical properties of these 3D structures in accordance with the specific clinical applications.

References

- [1] World Health Organization, “WHO | Life expectancy,” 2018. Cited on page 1.
- [2] G. Office of the Surgeon, “Reports of the Surgeon General,” tech. rep., Rockville (MD), 2004. Cited on pages 1, 5, 7, 9, and 10.
- [3] G. M. Bran, J. Stern-Straeter, K. Hormann, F. Riedel, and U. R. Goessler, “Apoptosis in bone for tissue engineering,” *Arch Med Res*, vol. 39, no. 5, pp. 467–482, 2008. Cited on pages 1, 3, 5, and 10.
- [4] H. Petite, V. Viateau, W. Bensaid, A. Meunier, C. de Pollak, M. Bourguignon, K. Oudina, L. Sedel, and G. Guillemain, “Tissue-engineered bone regeneration,” *Nat Biotechnol*, vol. 18, no. 9, pp. 959–963, 2000. Cited on page 1.
- [5] C. Van Blitterswijk, *Tissue engineering*. Boston, MA: Elsevier, 2014. Cited on pages 1 and 3.
- [6] E. M. Younger and M. W. Chapman, “Morbidity at bone graft donor sites.,” *Journal of orthopaedic trauma*, vol. 3, no. 3, pp. 192–195, 1989. Cited on pages 1 and 2.
- [7] W. Wang and K. W. Yeung, “Bone grafts and biomaterials substitutes for bone defect repair: A review,” *Bioactive Materials*, vol. 2, no. 4, pp. 224–247, 2017. Cited on page 1.
- [8] B. Stevens, Y. Yang, A. Mohandas, B. Stucker, and K. Nguyen, *A review of materials, fabrication methods, and strategies used to enhance bone regeneration in engineered bone tissues*, vol. 85. 2008. Cited on page 1.
- [9] V. Campana, G. Milano, E. Pagano, M. Barba, C. Cicione, G. Salonna, W. Lattanzi, and G. Logroscino, “Bone substitutes in orthopaedic surgery: from basic science to clinical practice,” *Journal of Materials Science: Materials in Medicine*, vol. 25, no. 10, pp. 2445–2461, 2014. Cited on page 1.
- [10] B. Grafts, S. M. Size, R. Summary, I. Insights, S. Affairs, U. Nations, and P. Division, “Bone Grafts and Substitutes Market Size, Share & Trends Analysis Report By Material Type (Natural, Synthetic), By Application Type (Spinal Fusion, Craniomaxillofacial, Long Bone), By Region, And Segment Forecasts, 2018 - 2025,” tech. rep., 2018. Cited on page 2.
- [11] L. Roseti, V. Parisi, M. Petretta, C. Cavallo, G. Desando, I. Bartolotti, and B. Grigolo, “Scaffolds for Bone Tissue Engineering: State of the art and new perspectives,” *Materials Science and Engineering C*, vol. 78, pp. 1246–1262, 2017. Cited on page 1.
- [12] A. Oryan, S. Alidadi, A. Moshiri, and N. Maffulli, “Bone regenerative medicine : classic options , novel strategies , and future directions,” pp. 1–27, 2014. Cited on page 2.

- [13] S. B. Manesh, R. O. Samani, and S. B. Manesh, "Ethical Issues of Transplanting Organs from Transgenic Animals into Human Beings," vol. 16, no. 3, pp. 353–360, 2014. Cited on page 2.
- [14] R. F. Fernández, C. Bucchi, P. Navarro, V. Beltrán, and E. Borie, "Bone grafts utilized in dentistry : an analysis of patients ' preferences," *BMC Medical Ethics*, pp. 1–6, 2015. Cited on page 2.
- [15] H. Melo and C. Branda, "Ethical and legal issues in xenotransplantation," vol. 15, no. 5, 2001. Cited on page 2.
- [16] M. Mucalo, *Hydroxyapatite (HAp) for biomedical applications*. No. number 95, Amsterdam ; Boston: Elsevier/Woodhead Publishing, Woodhead Publishing is an imprint of Elsevier, 2015. Cited on pages 5, 12, 14, and 15.
- [17] R. R. Seeley, P. Tate, and T. D. Stephens, *Anatomy & physiology*. Dubuque, IA: McGraw-Hill, 8th ed., 2008. Cited on pages 5, 6, 7, and 10.
- [18] B. Clarke, "Normal bone anatomy and physiology," *Clin J Am Soc Nephrol*, vol. 3 Suppl 3, pp. S131–9, 2008. Cited on pages 5, 7, 8, and 9.
- [19] G. H. Bourne, *The biochemistry and physiology of bone*. New York,: Academic Press, 2d ed., 1971. Cited on pages 5, 6, and 7.
- [20] D. J. Hadjidakis and I. I. Androulakis, "Bone remodeling," *Ann N Y Acad Sci*, vol. 1092, pp. 385–396, 2006. Cited on pages 5, 6, 7, and 9.
- [21] A. G. Robling, A. B. Castillo, and C. H. Turner, "Biomechanical and molecular regulation of bone remodeling," *Annu Rev Biomed Eng*, vol. 8, pp. 455–498, 2006. Cited on pages 7, 8, and 9.
- [22] Manolagas SC, "Birth and death of bone cells: basic regulatory mechanisms and implications for the pathogenesis and treatment of osteoporosis," *Endocrine Reviews*, vol. 21, no. January, pp. 115–137, 2000. Cited on page 8.
- [23] G. A. Rodan and T. J. Martin, "Therapeutic approaches to bone diseases," *Science*, vol. 289, no. 5484, pp. 1508–1514, 2000. Cited on page 10.
- [24] W. D. Callister and D. G. Rethwisch, *Materials science and engineering : an introduction*. Hoboken, NJ: John Wiley & Sons, 8th ed., 2010. Cited on page 11.
- [25] A. R. Studart, U. T. Gonzenbach, E. Tervoort, and L. J. Gauckler, "Processing routes to macroporous ceramics: A review," *Journal of the American Ceramic Society*, vol. 89, no. 6, pp. 1771–1789, 2006. Cited on pages 11, 12, 13, and 14.
- [26] T. Ohji and M. Fukushima, "Macro-porous ceramics: processing and properties," *International Materials Reviews*, vol. 57, no. 2, pp. 115–131, 2012. Cited on pages 11, 12, and 14.
- [27] G. Jean, V. Sciamanna, M. Demuynck, F. Cambier, and M. Gonon, "Macroporous ceramics: Novel route using partial sintering of alumina-powder agglomerates obtained by spray-drying," *Ceramics International*, vol. 40, no. 7, pp. 10197–10203, 2014. Cited on pages 12 and 14.
- [28] D. W. Hutmacher, M. Sittinger, and M. V. Risbud, "Scaffold-based tissue engineering: Rationale for computer-aided design and solid free-form fabrication systems," *Trends in Biotechnology*, vol. 22, no. 7, pp. 354–362, 2004. Cited on page 14.

- [29] C. J. Damien and J. R. Parsons, "Bone-Graft and Bone-Graft Substitutes - a Review of Current Technology and Applications," *Journal of Applied Biomaterials*, vol. 2, no. 3, pp. 187–208, 1991. Cited on pages [14](#) and [15](#).
- [30] M. Vallet-Regi and J. M. Gonzalez-Calbet, "Calcium phosphates as substitution of bone tissues," *Progress in Solid State Chemistry*, vol. 32, no. 1-2, pp. 1–31, 2004. Cited on page [15](#).
- [31] V. S. Gshalaev and A. C. Demirchan, *Hydroxyapatite: Synthesis, properties and applications*. 2013. Cited on pages [14](#) and [15](#).
- [32] F. Barrere, C. A. van Blitterswijk, and K. de Groot, "Bone regeneration: molecular and cellular interactions with calcium phosphate ceramics," *Int J Nanomedicine*, vol. 1, no. 3, pp. 317–332, 2006. Cited on pages [14](#) and [16](#).
- [33] S. Koutsopoulos, "Synthesis and characterization of hydroxyapatite crystals: A review study on the analytical methods," *Journal of Biomedical Materials Research*, vol. 62, no. 4, pp. 600–612, 2002. Cited on page [14](#).
- [34] S. H. Li, J. R. de Wijn, P. Layrolle, and K. de Groot, "Novel method to manufacture porous hydroxyapatite by dual-phase mixing," *Journal of the American Ceramic Society*, vol. 86, no. 1, pp. 65–72, 2003. Cited on page [14](#).
- [35] D. S. Metsger, T. D. Driskell, and J. R. Paulsrud, "Tricalcium Phosphate Ceramic - a Resorbable Bone Implant - Review and Current Status," *Journal of the American Dental Association*, vol. 105, no. 6, pp. 1035–1038, 1982. Cited on page [15](#).
- [36] S. Lohfeld, V. Barron, and P. E. McHugh, "Biomodels of bone: a review," *Ann Biomed Eng*, vol. 33, no. 10, pp. 1295–1311, 2005. Cited on pages [16](#), [17](#), [18](#), [19](#), and [20](#).
- [37] X. Yan and P. Gu, "A review of rapid prototyping technologies and systems," *Computer-Aided Design*, vol. 28, no. 4, pp. 307–318, 1996. Cited on page [16](#).
- [38] American Society for Testing and Materials, "ASTM F42/ISO TC 261 Develops Additive Manufacturing Standards." Cited on page [16](#).
- [39] Loughborough University Additive Manufacturing Research Group, "The 7 categories of Additive Manufacturing | Additive Manufacturing Research Group | Loughborough University," 2016. Cited on pages [16](#), [17](#), and [18](#).
- [40] J. Y. Lee, J. An, and C. K. Chua, "Fundamentals and applications of 3D printing for novel materials," *Applied Materials Today*, vol. 7, pp. 120–133, 2017. Cited on pages [16](#) and [17](#).
- [41] E. MacDonald and R. Wicker, "Multiprocess 3D printing for increasing component functionality," *Science*, vol. 353, no. 6307, 2016. Cited on pages [16](#) and [17](#).
- [42] P. S. D'Urso, R. L. Atkinson, M. W. Lanigan, W. J. Earwaker, I. J. Bruce, A. Holmes, T. M. Barker, D. J. Effeney, and R. G. Thompson, "Stereolithographic (SL) biomodelling in craniofacial surgery," *Br J Plast Surg*, vol. 51, no. 7, pp. 522–530, 1998. Cited on page [17](#).
- [43] S. Gomez, M. D. Vlad, J. Lopez, and E. Fernandez, "Design and properties of 3D scaffolds for bone tissue engineering," *Acta Biomaterialia*, vol. 42, pp. 341–350, 2016. Cited on page [18](#).

- [44] F. Rengier, A. Mehndiratta, H. von Tengg-Kobligk, C. M. Zechmann, R. Unterhinninghofen, H. U. Kauczor, and F. L. Giesel, "3D printing based on imaging data: review of medical applications," *Int J Comput Assist Radiol Surg*, vol. 5, no. 4, pp. 335–341, 2010. Cited on pages 19 and 20.
- [45] H. Seitz, W. Rieder, S. Irsen, B. Leukers, and C. Tille, "Three-dimensional printing of porous ceramic scaffolds for bone tissue engineering," *Journal of Biomedical Materials Research - Part B Applied Biomaterials*, vol. 74, no. 2, pp. 782–788, 2005. Cited on page 19.
- [46] X. Li, Y. F. Feng, C. T. Wang, G. C. Li, W. Lei, Z. Y. Zhang, and L. Wang, "Evaluation of Biological Properties of Electron Beam Melted Ti6Al4V Implant with Biomimetic Coating In Vitro and In Vivo," *PLoS ONE*, vol. 7, no. 12, 2012. Cited on page 19.
- [47] S. Bose, S. Vahabzadeh, and A. Bandyopadhyay, "Bone tissue engineering using 3D printing," *Materials Today*, vol. 16, no. 12, pp. 496–504, 2013. Cited on pages 20 and 21.
- [48] C. Groth, N. D. Kravitz, P. E. Jones, J. W. Graham, and W. R. Redmond, "Three-dimensional printing technology," *Journal of clinical orthodontics : JCO*, vol. 48, no. 8, pp. 475–85, 2014. Cited on pages 21 and 22.
- [49] R. Felzmann, S. Gruber, G. Mitteramskogler, P. Tesavibul, A. R. Boccaccini, R. Liska, and J. Stampfl, "Lithography-based additive manufacturing of cellular ceramic structures," *Advanced Engineering Materials*, vol. 14, no. 12, pp. 1052–1058, 2012. Cited on page 21.
- [50] think 3D, "Digital Light Processing (DLP) Technology Overview | think3D," 2016. Cited on page 21.
- [51] T. Billiet, M. Vandenhoute, J. Schelfhout, S. Van Vlierberghe, and P. Dubruel, "A review of trends and limitations in hydrogel-rapid prototyping for tissue engineering," *Biomaterials*, vol. 33, no. 26, pp. 6020–6041, 2012. Cited on page 21.
- [52] H. N. Chia and B. M. Wu, "Recent advances in 3D printing of biomaterials," *J Biol Eng*, vol. 9, p. 4, 2015. Cited on page 21.
- [53] M. Griffith, A. J. Lightman, R. P. Chartoff, E. Sachs, M. S. Conference, A. Arbor, R. U. S. A. Data, A. C. Young, M. L. Griffith, J. W. Halloran, L. Manufacturing, X. Shan, N. Nakajima, M. J. Cima, S. Freeform, and F. Proceedings, "Stereolithography resin for rapid prototyping of ceramics and metals," 2000. Cited on pages 23, 42, and 43.
- [54] S. Padilla and R. Garcı, "Hydroxyapatite suspensions as precursors of pieces obtained by gelcasting method," vol. 24, pp. 2223–2232, 2004. Cited on page 23.
- [55] B. Tyliczszak, "Stabilization of Ceramics Particles with Anionic Polymeric Dispersants Stabilization of Ceramics Particles with Anionic Polymeric Dispersants," no. March 2014, 2012. Cited on page 23.
- [56] T. P. Niraula, A. Bhattarai, and S. K. Chatterjee, "Sodium dodecyl sulphate : A very useful surfactant for Scientific Invetigations Sodium dodecylsulphate : A very useful Surfactant for Scientific Investigations," no. January, 2014. Cited on page 23.
- [57] E. Salahi and A. Rajabi, "Fabrication and Characterization of Hydroxyapatite-Carbon Nano Tubes Composites," vol. 2, no. 4, pp. 41–45, 2016. Cited on page 23.

- [58] A. Kolodziejczak-radzimska and M. Samuel, "Synthesis of hydroxyapatite in the presence of anionic surfactant," vol. 50, no. 1, 2014. Cited on page 23.
- [59] R. M. Dukali, "Electrospinning of the laser dye rhodamine B-doped poly (methyl methacrylate) nanofibers," vol. 79, no. 7, pp. 867–880, 2014. Cited on page 35.
- [60] G. Duan, A. C. Zhang, A. Li, X. Yang, L. Lu, and X. Wang, "Preparation and Characterization of Mesoporous Zirconia Made by Using a Poly (methyl methacrylate) Template," pp. 118–122, 2008. Cited on page 35.
- [61] E. M. Carlisle, "In vivo requirement for silicon in articular cartilage and connective tissue formation in the chick.," *The Journal of nutrition*, vol. 106, no. 4, pp. 478–84, 1976. Cited on page 38.
- [62] L. Mao, L. Xia, J. Chang, J. Liu, L. Jiang, C. Wu, and B. Fang, "The synergistic effects of Sr and Si bioactive ions on osteogenesis, osteoclastogenesis and angiogenesis for osteoporotic bone regeneration," *Acta Biomaterialia*, vol. 61, pp. 217–232, 2017. Cited on page 38.
- [63] S. H. Huang, Y. J. Chen, C. T. Kao, C. C. Lin, T. H. Huang, and M. Y. Shie, "Physicochemical properties and biocompatibility of silica doped β -tricalcium phosphate for bone cement," *Journal of Dental Sciences*, vol. 10, no. 3, pp. 282–290, 2015. Cited on page 38.
- [64] M. Y. Shie, S. J. Ding, and H. C. Chang, "The role of silicon in osteoblast-like cell proliferation and apoptosis," *Acta Biomaterialia*, vol. 7, no. 6, pp. 2604–2614, 2011. Cited on page 38.
- [65] N. Shadjou and M. Hasanzadeh, "Bone tissue engineering using silica-based mesoporous nanobiomaterials:Recent progress," *Materials Science and Engineering C*, vol. 55, pp. 401–409, 2015. Cited on page 38.
- [66] C. Knabe, D. Adel-Khattab, W. D. Hübner, F. Peters, T. Knauf, B. Peleska, D. Barnewitz, A. Genzel, R. Kusserow, F. Sterzik, M. Stiller, and C. Müller-Mai, "Effect of silicon-doped calcium phosphate bone grafting materials on bone regeneration and osteogenic marker expression after implantation in the ovine scapula," *Journal of Biomedical Materials Research - Part B Applied Biomaterials*, pp. 1–21, 2018. Cited on page 38.
- [67] Database, Inorganic Crystal Structure, "ICSD: Home." Cited on page 41.
- [68] A. Cüneyt Taş, F. Korkusuz, M. Timuçin, and N. Akkaş, "An investigation of the chemical synthesis and high-temperature sintering behaviour of calcium hydroxyapatite (HA) and tricalcium phosphate (TCP) bioceramics," *Journal of Materials Science: Materials in Medicine*, vol. 8, no. 2, pp. 91–96, 1997. Cited on page 42.
- [69] A. Ogoşe, T. Hotta, H. Kawashima, N. Kondo, W. Gu, T. Kamura, and N. Endo, "Comparison of hydroxyapatite and beta tricalcium phosphate as bone substitutes after excision of bone tumors," *Journal of Biomedical Materials Research - Part B Applied Biomaterials*, vol. 72, no. 1, pp. 94–101, 2005. Cited on page 42.
- [70] P. Wongwitwichot, J. Kaewsrichan, K. H. Chua, and B. H.I. Ruszymah, "Comparison of TCP and TCP/HA Hybrid Scaffolds for Osteoconductive Activity," *The Open Biomedical Engineering Journal*, vol. 4, no. 1, pp. 279–285, 2010. Cited on page 42.
- [71] R. Z. LeGeros, "Properties of osteoconductive biomaterials: Calcium phosphates," *Clinical Orthopaedics and Related Research*, no. 395, pp. 81–98, 2002. Cited on page 42.

- [72] A. Monshi, A. Daniels, A. Doostmohammadi, R. Salehi, U. Pieleles, M. Fathi, and S. Karbasi, "Preparation, chemistry and physical properties of bone-derived hydroxyapatite particles having a negative zeta potential," *Materials Chemistry and Physics*, vol. 132, no. 2-3, pp. 446–452, 2011. Cited on page 42.
- [73] A. B. Metzner, "Rheology of Suspensions in Polymeric Liquids," *Journal of Rheology*, vol. 29, no. 6, pp. 739–775, 2002. Cited on page 42.
- [74] B. J. Konijn, O. B. Sanderink, and N. P. Kruijt, "Experimental study of the viscosity of suspensions: Effect of solid fraction, particle size and suspending liquid," *Powder Technology*, vol. 266, pp. 61–69, 2014. Cited on page 43.
- [75] L. Yubao, C. P. A. T. Klein, Z. Xingdong, and K. D. Groat, "Relationship between the colour change of hydroxyapatite and the trace element manganese," *Biomaterials*, vol. 14, no. 13, pp. 969–972, 1993. Cited on page 44.
- [76] G. Buckton and A. E. Beezer, "The relationship between particle size and solubility," *International Journal of Pharmaceutics*, vol. 82, pp. R7–R10, may 1992. Cited on page 44.
- [77] G. Muralithran and S. Ramesh, "The effects of sintering temperature on the properties of hydroxyapatite," *Ceramics International*, vol. 26, no. 2, pp. 221–230, 2000. Cited on pages 45 and 46.
- [78] S. R. Kim, J. H. Lee, Y. T. Kim, D. H. Riu, S. J. Jung, Y. J. Lee, S. C. Chung, and Y. H. Kim, "Synthesis of Si,Mg substituted hydroxyapatites and their sintering behaviors.pdf," *Biomaterials*, vol. 24, pp. 1389–1398, 2003. Cited on page 46.
- [79] J. Darsell, H. Hosick, A. Bandyopadhyay, M. Kintner, and S. Bose, "Pore size and pore volume effects on alumina and TCP ceramic scaffolds," *Materials Science and Engineering: C*, vol. 23, no. 4, pp. 479–486, 2002. Cited on page 46.
- [80] J. C. Elliot, *Structure and Chemistry of the Apatites and Other Calcium Orthophosphates*. Elsevier, 1994. Cited on page 47.
- [81] Q. Tan, S. Li, J. Ren, and C. Chen, "Fabrication of porous scaffolds with a controllable microstructure and mechanical properties by porogen fusion technique," *International Journal of Molecular Sciences*, vol. 12, no. 2, pp. 890–904, 2011. Cited on page 48.
- [82] A. Lemos, J. D. Santos, and J. M. F. Ferreira, "New Method for the Incorporation of Soluble Bioactive Glasses to Reinforce Porous HA Structures," *Key Engineering Materials*, vol. 254–256, pp. 1033–1036, 2009. Cited on page 48.
- [83] Y. Muslim, J. Knowles, and J. Howlett, "Mechanical Properties of Glass Reinforced Hydroxyapatite," *Annals of Dentistry*, vol. 12, no. 1, pp. 31–36, 2018. Cited on page 48.
- [84] K. S. Tenhuisen and P. W. Brown, "Formation of calcium-deficient hydroxyapatite from a tricalcium phosphate," vol. 19, pp. 2209–2217, 1998. Cited on page 51.